

UNCLASSIFIED

AD NUMBER

AD892628

LIMITATION CHANGES

TO:

Approved for public release; distribution is unlimited.

FROM:

Distribution authorized to U.S. Gov't. agencies only; Test and Evaluation; FEB 1972. Other requests shall be referred to Air Force Weapons Laboratory, Attn: SYS, Kirtland AFB, NM 87117.

AUTHORITY

AFWL ltr, 29 Apr 1985

THIS PAGE IS UNCLASSIFIED

AD E92628

AUTHORITY: AFWL 17,29 APR 85

AD 892628



AD No. \_\_\_\_\_  
DDC FILE COPY

## ELECTRON BEAM FRACTURING OF HARD ROCK

Merle E. Hanson  
Ronald J. Shaffer  
Allan R. Sanford

New Mexico Institute of Mining and Technology

TECHNICAL REPORT NO. AFWL-TR-71-143

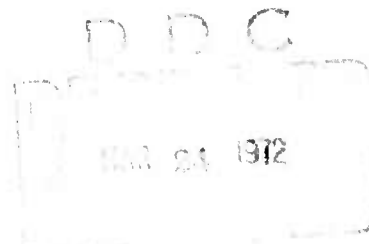
February 1972

AIR FORCE WEAPONS LABORATORY

Air Force Systems Command  
Kirtland Air Force Base  
New Mexico

Details of illustrations in  
this document may be better  
studied on microfilm.

gr



AIR FORCE WEAPONS LABORATORY  
Air Force Systems Command  
Kirtland Air Force Base  
New Mexico 87117

B

When US Government drawings, specifications, or other data are used for any purpose other than a definitely related Government procurement operation, the Government thereby incurs no responsibility nor any obligation whatsoever, and the fact that the Government may have formulated, furnished, or in any way supplied the said drawings, specifications, or other data, is not to be regarded by implication or otherwise, as in any manner licensing the holder or any other person or corporation, or conveying any rights or permission to manufacture, use, or sell any patented invention that may in any way be related thereto.

DO NOT RETURN THIS COPY. RETAIN OR DESTROY.

ELECTRON BEAM FRACTURING OF HARD ROCK

Merle E. Hanson

Ronald J. Shaffer

Allan R. Sanford

New Mexico Institute of Mining and Technology

TECHNICAL REPORT NO. AFWL-TR-71-143

Distribution limited to US Government agencies only because of test and evaluation (February 1972). Other requests for this document must be referred to AFWL (SYS), Kirtland AFB, NM 87117.

FOREWORD

This report was prepared by the New Mexico Institute of Mining and Technology, Socorro, New Mexico, under Contract F29601-71-C-0017, and was funded by the Advanced Research Projects Agency under ARPA Order Number 1690.

Inclusive dates of research were 13 October 1970 through 13 December 1971. The report was submitted 12 January 1972 by the Air Force Weapons Laboratory Project Officer, Dr. Daniel N. Payton III (SYS).

This report has been reviewed and is approved.



DANIEL N. PAYTON III  
Project Officer



RICHARD S. BURNS  
Major, USAF  
Chief, Simulation Branch



CARL B. HILLAND  
Lt Colonel, USAF  
Chief, Technology Division

## ABSTRACT

### (Distribution Limitation Statement B)

An experimental and analytical investigation has been conducted to determine if a moving pressure source can drive a fracture parallel to a free surface. The research was conducted to determine the technical feasibility of a hard-rock mining technique using a high-energy electron beam to create the moving pressure source. By controlling the electron beam sweep orientation and sweep velocity across a rock face, a minimum-energy rock-breaking procedure can be envisioned. The two-dimensional analytical technique used could not simulate fracture branching phenomena. However, the analysis of the dynamic stress field produced by a programmed straight fracture did indicate that branch fractures would occur in the region of the pressure source. If these branch fractures were subsequently pressurized, it might be possible to propagate the fracture parallel to the free surface. The experimental investigations showed 1) that slowing the detonation velocity does cause different fracture characteristics but does not necessarily increase the amount of damage; 2) that fracture always occurred to some extent directly below the line of detonation (perpendicular to the free surface) where pressure was applied; 3) that explosive detonating cord probably cannot be used to simulate a high energy electron beam; and 4) that a ripple type detonation will not produce sufficient energy on the surface of the test specimen. The detonating cord had to be applied in a snaked geometry on the surface to provide the slow phase velocities and the high energy densities. Some correlation between experiment and analysis can be made in the branch fracture pattern and the damage on the fracture initiation surface.

## CONTENTS

SECTION		PAGE
I	Introduction	1
II	Method	3
	Introduction	3
	Analytical Procedure	3
	Experimental Procedure	6
III	Analytical Results	9
	Introduction	9
	Computer Simulations	9
	Summary and Conclusions	24
IV	Experimental Results	26
	Description of Experiments	26
	Discussion and Conclusions of Experiments	37
V	Summary	40
	References	42



## LIST OF ILLUSTRATIONS

FIGURE		PAGE
1	The pressure profile simulated within the fracture surfaces. The dimensions of the pressure source were used with a 1 centimeter square Lagrangian grid.	4
2	The geometry of the numerically simulated problem	4
3	Snaked explosive cord taped in place over a .61-meter length previous to stemming with mud. The results of this experiment are shown in Figure 16a.	8
4	Elapsed time output from oscilloscope. At .1 msec per centimeter the display shows .38 msec between ionizations on a 2.43-meter explosive cord. The velocity of detonation is calculated as 6400 m/sec.	8
5a	The magnitude of the stress difference, $ \sigma_1 - \sigma_2 $ , for the fracture velocity $0.25C_1$ and the early time slice. The fracture length is 3 centimeters and the x and y axes on the plot are spatial coordinates in centimeters. The fracture originated at $x = 1$ and $y = 5-1/2$ centimeters. The minimum contour (1) is 0.5 and the contour interval is 0.5 kilobar.	13
5b	The contours of the dilatation for the fracture velocity of $0.25C_1$ and the early time slice. The fracture length is 3 centimeters and the x and y axes on the plot are spatial coordinates in centimeters. The fracture originated at $x = 1$ and $y = 5-1/2$ centimeters. The contour of zero dilatation is 4 with a contour interval of 0.003.	13
6a	The maximum principal tensor axes for the fracture velocity of $0.25C_1$ and the early time slice. The fracture length is 3 centimeters and the x and y axes on the plot are spatial coordinates in centimeters. The fracture is shown as the rough line and the position of the pressure source is shown by the double lines, one on each side of the fracture near the tip.	14

FIGURE	LIST OF ILLUSTRATIONS, Continued	PAGE
6b	The magnitude of the stress difference, $ \sigma_1 - \sigma_2 $ , for the fracture velocity $0.35C_1$ and the early time slice. The fracture length is 4 centimeters and the x and y axes on the plot are spatial coordinates in centimeters. The fracture originated at $x = 1$ and $y = 5-1/2$ centimeters. The minimum contour (1) is 0.5 kilobar and the contour interval is 0.5 kilobar.	14
7a	The contours of dilatation for the fracture velocity of $0.35C_1$ and the early time slice. The fracture length is 4 centimeters and the x and y axes on the plot are spatial coordinates in centimeters. The fracture originated at $x = 1$ and $y = 5-1/2$ centimeters. The contour of zero dilatation is 4 with a contour interval of 0.003.	15
7b	The maximum principal tensor axes for the fracture velocity of $0.35C_1$ and the early time slice. The fracture length is 4 centimeters and the x and y axes on the plot are the spatial coordinates in centimeters. The fracture is shown as the rough line and the position of the pressure source is shown by the double lines, one on each side of the fracture near the tip.	15
8a	The magnitude of the stress difference $ \sigma_1 - \sigma_2 $ for the fracture velocity of $0.45C_1$ and the early time slice. The fracture length is 5 centimeters and the x and y axes on the plots are the spatial coordinates in centimeters. The fracture originated at $x = 1$ and $y = 5-1/2$ centimeters. The minimum contour (1) is 0.5 kilobar and the contour interval is 0.5 kilobar.	16
8b	The contours of dilatation for the fracture velocity of $0.45C_1$ and the early time slice. The fracture length is 5 centimeters and the x and y axes on the plot are spatial coordinates in centimeters. The fracture originated at $x = 1$ and $y = 5-1/2$ centimeters. The contour of zero dilatation is 4 and the contour interval is 0.003.	16

# LIST OF ILLUSTRATIONS, Continued

## FIGURE

## PAGE

- |     |  |    |
|-----|--|----|
| 9a  | The maximum principal tensor axes for the fracture velocity of $0.45C_1$ and the early time slice. The fracture length is 5 centimeters and the x and y axes on the plot are the spatial coordinates in centimeters. The fracture is shown as the rough line and the position of the pressure source is shown by the double lines, one on each side of the fracture near the tip.                    | 17 |
| 9b  | The magnitude of the stress difference, $ \sigma_1 - \sigma_2 $ , for the fracture velocity of $0.25C_1$ and the later time slice. The fracture length is 5 centimeters and the x and y axes on the plot are the spatial coordinates in centimeters. The fracture originated at $x = 1$ and $y = 5-1/2$ centimeters. The minimum contour (1) is 0.5 kilobar and the contour interval is 0.5 kilobar. | 17 |
| 10a | The contours of dilatation for the fracture velocity of $0.25C_1$ and the later time slice. The fracture length is 5 centimeters and the x and y axes on the plot are the spatial coordinates in centimeters. The fracture originated at $x = 1$ and $y = 5-1/2$ centimeters. The contour of zero dilatation is 4 and the contour interval is 0.003.   | 18 |
| 10b | The maximum principal tensor axes for the fracture velocity of $0.25C_1$ and the later time slice. The fracture length is 5 centimeters and the x and y axes on the plot are the spatial coordinates in centimeters. The fracture is shown as the rough line and the position of the pressure source is shown by the double lines, one on each side of the fracture near the tip.                    | 18 |
| 11a | The magnitude of the stress difference $ \sigma_1 - \sigma_2 $ for the fracture velocity of $0.35C_1$ and the later time slice. The fracture length is 7 centimeters and the x and y axes on the plot are the spatial coordinates in centimeters. The fracture originated at $x = 1$ and $y = 5-1/2$ centimeters. The minimum contour (1) is 0.5 kilobars and the contour interval is 0.5 kilobar.   | 19 |

# LIST OF ILLUSTRATIONS, Continued

FIGURE		PAGE
11b	The contours of dilatation for the fracture velocity of $0.35C_1$ and the later time slice. The fracture length is 7 centimeters and the x and y axes on the plot are the spatial coordinates in centimeters. The fracture originated at $x = 1$ and $y = 5-1/2$ centimeters. The contour of zero dilatation is 4 and the contour interval is 0.003.	19
12a	The maximum principal tensor axes for the fracture velocity of $0.35C_1$ and the later time slice. The fracture length is 7 centimeters and the x and y axes on the plot are the spatial coordinates in centimeters. The fracture is shown as the rough line and the position of the pressure source is shown by the double lines, one on each side of the fracture near the tip.	20
12b	The magnitude of the stress difference, $ \sigma_1 - \sigma_2 $ , for the fracture velocity of $0.45C_1$ and the later time slice. The fracture length is 9 centimeters and the x and y axes on the plot are the spatial coordinates in centimeters. The minimum contour (1) is 0.5 kilobar and the contour interval is 0.5 kilobar.	20
13a	The contours of dilatation for the fracture velocity of $0.45C_1$ and the later time slice. The fracture length is 9 centimeters and the x and y axes on the plot are the spatial coordinates in centimeters. The fracture originated at $x = 1$ and $y = 5-1/2$ centimeters. The contour of zero dilatation is 4 and the contour interval is 0.003.	21
13b	The maximum principal tensor axes for the fracture velocity of $0.45C_1$ and the later time slice. The fracture length is 9 centimeters and the x and y axes on the plot are the spatial coordinates in centimeters. The fracture is shown as the rough line and the position of the pressure source is shown by the double lines, one on each side of the fracture near the tip.	21

## LIST OF ILLUSTRATIONS, Continued

FIGURE		PAGE
14a	The magnitude of the stress difference, $ \sigma_1 - \sigma_2 $ , for the grid center fracture at the early time slice and a fracture velocity of $0.35C_1$ . The fracture length is 4 centimeters and the x and y axes on the plot are the spatial coordinates in centimeters. The fracture originated at $x = 1$ and $y = 15\text{-}1/2$ centimeters. The minimum contour (1) is 0.5 kilobar and the contour interval is 0.5 kilobar.	22
14b	The contours of dilatation for the grid center fracture at the early time slice and a fracture velocity of $0.35C_1$ . The fracture length is 4 centimeters and the x and y axes on the plot are the spatial coordinates in centimeters. The fracture originated at $x = 1$ and $y = 15\text{-}1/2$ centimeters. The contour of zero dilatation is 4 and the contour interval is 0.003.	22
15	The maximum principal tensor axes for the grid center fracture at the early time slice and a fracture velocity of $0.35C_1$ . The fracture length is 4 centimeters and the x and y axes on the plot are the spatial coordinates in centimeters. The fracture is shown as the rough line and the position of the pressure source is shown by the double lines, one on each side of the fracture near the tip.	23
16a	Explosive density was 2000 grains/meter with V equal to 2100 meters/second.	28
16b	Explosive density was 2000 grains/meter with V equal to 6400 meters/second.	28
17a	Explosive density was 2000 grains/meter with V equal to 2100 meters/second.	29
17b	Explosive density was 2000 grains/meter with V equal to 6400 meters/second.	29
18a	Explosive density was 2000 grains/meter with V equal to 2100 meters/second.	30
18b	Explosive density was 2000 grains/meter with V equal to 6400 meters/second.	30
19a	Explosive density was 2600 grains/meter with V equal to 1600 meters/second.	32

# LIST OF ILLUSTRATIONS, Continued

FIGURE		PAGE
19b	Explosive density was 2600 grains/meter with V equal to 6400 meters/second.	32
20a	Explosive density was 2600 grains/meter with V equal to 1600 meters/second.	33
20b	Explosive density was 2600 grains/meter with V equal to 6400 meters/second.	33
21a	Explosive density was 2600 grains/meter with V equal to 1600 meters/second.	34
21b	Explosive density was 2600 grains/meter with V equal to 6400 meters/second.	34
22a	Explosive density was 1600 grains/meter with V equal to 5000 meters/second.	35
22b	Explosive density was 1600 grains/meter with V equal to 1300 meters/second.	35
23a	Explosive density was 1600 grains/meter with V equal to 1300 meters/second.	36
23b	Explosive density was 1600 grains/meter with V equal to 1300 meters/second.	36

## SYMBOLS

$\lambda, \mu$	Lamé elastic constants
$\nu$	Poisson's ratio
$C_1$	Compressional wave speed of elastic material
$\sigma_1, \sigma_2$	Principal stresses
$V$	Fracture velocity

## SECTION I

### INTRODUCTION

Current methods for mining hard rock generally require drilling, loading, stemming, blasting and mucking operations. Large rotary cutting heads are also used to drill horizontal and vertical shafts in hard rock. These conventional techniques are not efficient in terms of total energy expended in the mining operation. It has been postulated that the creation and propagation of fractures in a controlled manner could utilize energy more efficiently and yield large mined tonnage rates.

Several studies (Reference 1, 2, and 3) have shown that the theoretical maximum velocity of a straight running tensile fracture is approximately  $0.39C_1$  for an ideal, homogeneous, isotropic material. Real materials will exhibit terminal velocities somewhat lower than this value (Reference 4, 5) because the inhomogeneties and anisotropies in the material will absorb some of the strain energy, thereby reducing the energy available to maintain the theoretical terminal velocity. The terminal fracture velocity is the maximum velocity at which the strain energy will be transported to the region surrounding the fracture tip and result in a stress configuration which is sympathetic to fracture propagation in a straight line. If a sufficient amount of energy can be supplied to the fracture surfaces at a velocity equal to the terminal velocity, it may be possible to break rock using a minimum energy. If the energy was applied at too low a velocity, energy around the crack would accumulate in an unwanted manner and be dissipated without breaking much rock. On the other hand, if energy was applied too fast, the energy



would not be supplied correctly to the region around the tip and the resulting stress field would not allow sympathetic propagation of the crack in the desired direction.

A high-energy electron beam can be used to produce a moving pressure source in the fracture surfaces behind a moving fracture tip. If enough power is directed toward a rock surface, an ablation of the rock will result in ablation gas pressures sufficient to cause the rock to fracture. With the electron beam, the power can be directed locally where fracture is required and not be distributed over the rock volume. Under these conditions, the energy requirements to break a unit mass of rock from the face are small compared to conventional rock breaking techniques. Because the power source supplies energy at a high rate, the electron beam can be phased to provide the energy at an optimum fracture velocity and produce large tonnages of rock from a face per unit time.

To properly utilize the created fractures, the moving pressure source will have to move parallel to a free surface. The driven fracture would then break off rock between the moving electron beam and the free surface through a proper choice of beam path, velocity and energy.

The feasibility of this concept is the subject of this report. The results of the analytical and experimental investigation are given. Since an electron beam of sufficient power was not available for the research, explosive detonating cord was used experimentally to simulate the electron beam generated pressure source.

## SECTION II

### METHOD

#### A. INTRODUCTION

The research on the electron beam mining technique was performed using both analytical and experimental techniques. Since continuous wave high-energy electron beams were not available and funding for the use of a high-energy electron beam was not included for this research, explosives were applied to simulate the moving pressure source.

#### B. ANALYTICAL PROCEDURE

A two-dimensional elastic hydrocode was applied to analyze the pressure-driven fracture. A complete description of the hydrocode and the difference forms are given in Reference 6. This code has been used to simulate dynamic fracture for earthquake source function studies, some examples of this research are given in References 1, 7, and 8. Some code development was performed to simulate the application of the electron beam moving pressure source to the elastic code. The shape of the pressure profile in the fracture surfaces is shown in Figure 1. The maximum pressure was taken as 5 kilobars.

Several fracture criteria were used in evaluating the results. In all cases, the fracture criteria predicted that the fracture would not occur at the tip, but behind the tip in the region near the maximum pressure of the pressure source. The orientation of the predicted fractures using all the failure criteria are off the fracture axis

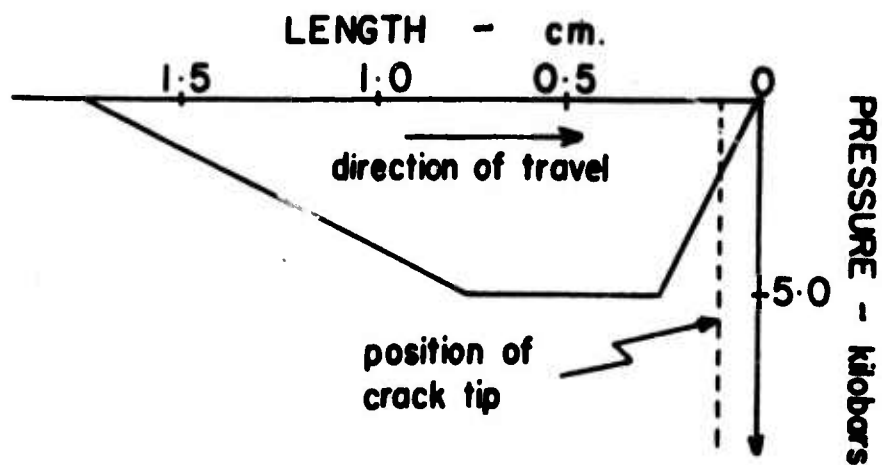


FIGURE 1 The pressure profile simulated within the fracture surfaces. The dimensions of the pressure source were used with a one centimeter square Lagrangian grid.

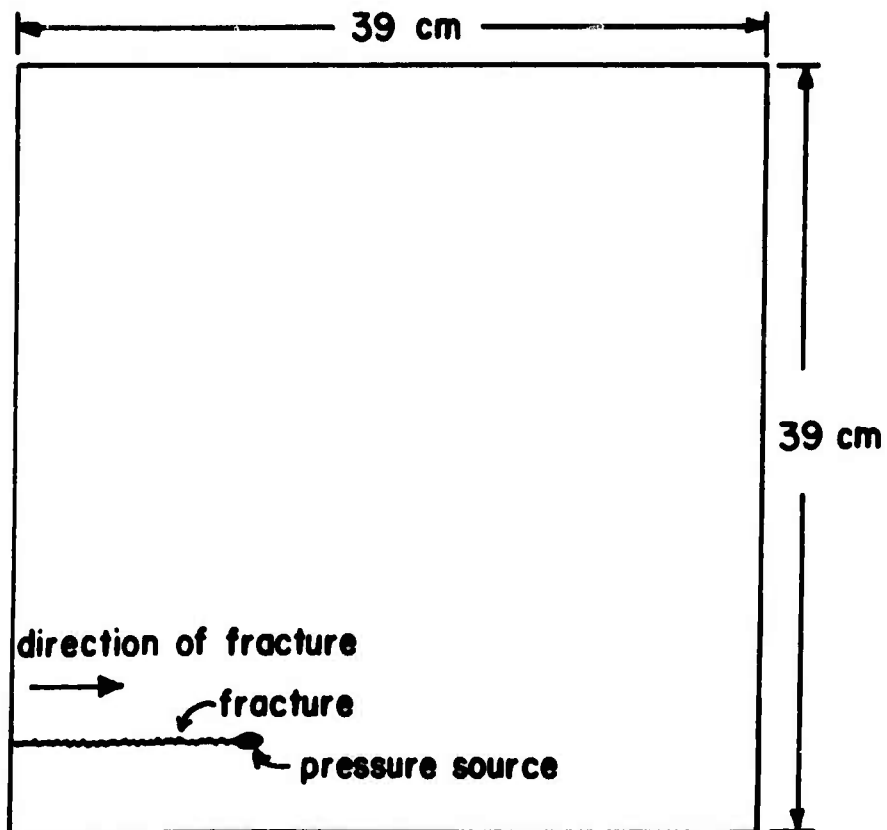


FIGURE 2 The geometry of the numerically simulated problem.

and thus would represent a branch fracturing phenomenon. Because the presently available codes cannot simulate a fracture that branches, the fracture was programmed to propagate at a given velocity in a straight line. The results shown in this report are simulations of single fractures driven at a constant speed.

Because branch fracturing was predicted to occur and an analysis allowing a branch fracture to occur would be more physically correct, further analysis of dynamic fracture phenomena was directed toward the development of a dynamic fracture branching code. The initial formulation has been completed and a Fortran IV version of the code has been written. Fortran "debugging" and checkout are not yet complete.

The geometry of the problems set up in the single fracture numerical code is shown on Figure 2. The ratio of the distance from the fracture to the near parallel free surface and from the fracture to the far parallel free surface for both the analysis and the experiments is approximately the same. The problem of a fracture propagating near a free surface was terminated before reflections from the far boundaries crossed the fracture. One centimeter square grids were chosen for the calculation. A total grid size of 40 x 40 was used. No damping was applied to the calculation. The Lamé elastic constants were taken as  $\lambda = \mu = 0.1$  megabar implying Poissons ratio  $\nu = 0.25$ . The Lamé constants are low for granite but Poissons ratio is approximately correct. The weaker Lamé constants result in lower body wave speeds and thus permit longer calculated time series before reflections from far boundaries can affect the region of interest.

### C. EXPERIMENTAL PROCEDURE

For the experiments, three blocks of granite (3 feet by 3 feet by ~ 4 feet) were obtained from New Mexico Granite, a quarry in Las Vegas, New Mexico. This granite appeared to be fairly uniform in texture and there were no apparent open cracks in the blocks. The blocks do exhibit some well healed joints or fractures. In some places, drill holes, approximately 1-inch in diameter penetrating a short distance into the blocks, can be seen on the surfaces. Apparently these holes were drilled to facilitate removal from the quarry area. The blocks were not polished nor were the ends perpendicular to the 4-foot dimension sawed.

The compressional wave speed of the granite material was determined from a core using a crystal driver and pickup. The nominal compressional wave-speed was 4330 m/sec and increased to 4880 m/sec under an axial stress of 0.265 kilobar. Very little hysteresis was noted in the wave speeds between the loading and unloading phases of the test.

Before the explosives were applied to these three granite test specimen, a phasing technique to slow the progress of the pressure wave across the test specimen was developed. Various scrap granite and in-place field rock on the New Mexico Tech test range were used during this phase of the experimental program. It was found that coiling the detonating cord in a plane perpendicular to the surface of the test specimen did not provide a sufficiently continuous pressure wave. This geometry left a pocked appearance on the surface of the test blocks. In addition, coiling the detonating cord reduced the amount of explosive which could be placed on the surface and would not provide sufficient energy on the surface. Of several other techniques tried, a method

where the explosive detonating cord was snaked flat against the surface within a given width was chosen. It was found that by placing some chips of lead between the loops of the snaked cord, the detonation wave in the cord would not bridge between the loops. Figure 3 is a photograph showing the snaked cord taped to the surface of a test specimen. In addition, a greater part of the energy was transferred to the surface and the noise was reduced by stemming with a small amount of mud. Grooves were used in some experiments but comparison of grooved and ungrooved rocks showed no observable difference between the results.

To verify that the detonation wave did not bridge between the loops and to get an accurate measurement of the velocity of the phased pressure source across the face of the rock, a velocity measuring system was developed. The system uses ionization probes placed along the explosive train. The circuit consists of a battery, a resistor, and a probe. No current flows in the circuit until the detonation wave crosses the probe. An oscilloscope connected across the resistor records the voltage changes.

An example of the output of the timing system is displayed on Figure 4. The sweep is from left to right with a sweep rate of 100  $\mu\text{sec}/\text{cm}$ . One ion probe was used for triggering the trace and another further down the explosive train. The velocity is calculated from trigger initiation to the probe ionization. The average velocity determined from this record is approximately 6400 m/sec.

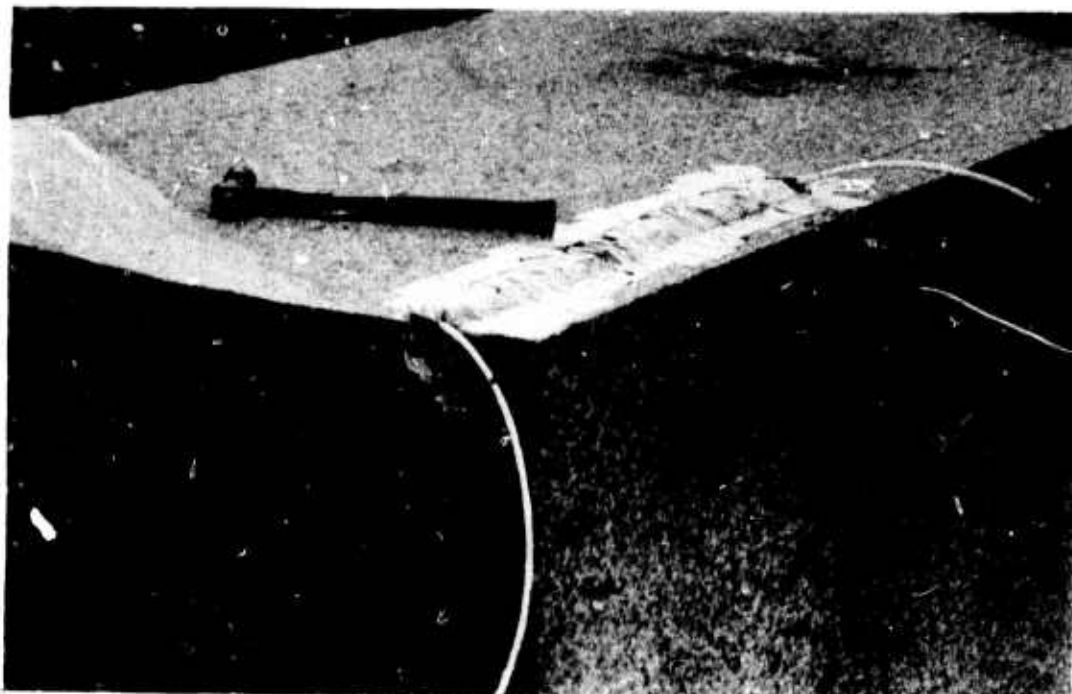


FIGURE 3. Snaked explosive cord taped in place over a 0.61 meter length previous to stemming with mud. The results of this experiment are shown in Figure 16a.

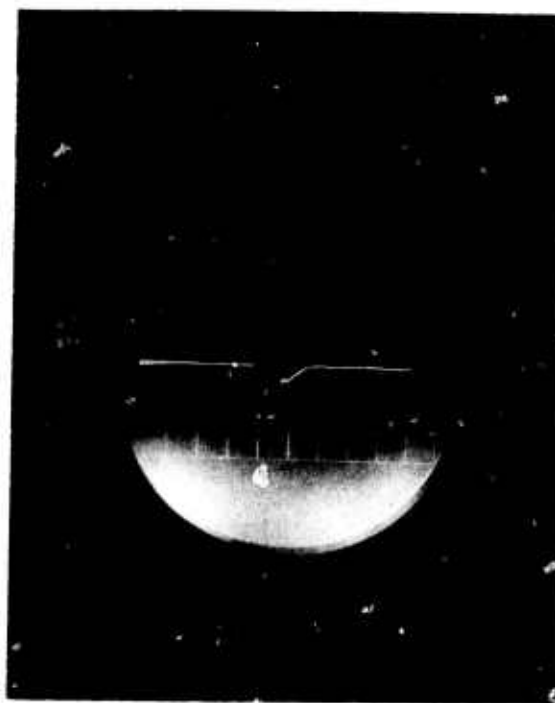


FIGURE 4. Elapsed time output from oscilloscope. At 0.1 msec per centimeter the display shows 0.38 msec between ionizations on a 2.43-meter explosive cord. The velocity of detonation is calculated as 6400 m/sec.

## SECTION III

### ANALYTICAL RESULTS

#### A. INTRODUCTION

Failure criteria, based on either a maximum distortional stress or a maximum tensional stress were used to determine the location and direction of fracture. The simulations, using a moving pressure source located just behind the fracture tip, indicated that a fracture would not continue forward in a straight line from the tip. The failure criteria predicted that (1) new fractures would occur behind the tip of the existing fracture on the surfaces adjacent to the pressure source, and (2) the directions of the new fracturing would not parallel the direction of the driven fracture.

#### B. COMPUTER SIMULATIONS

Because branch fracturing could not be handled with the existing code, the fracturing was assumed to form and propagate in a straight line at a prescribed velocity. A moving pressure source was positioned just behind the moving fracture tip in the two-dimensional calculations. Analysis of the constant-velocity, pressure-driven fractures were performed for three fracture velocities;  $0.25C_1$ ,  $0.35C_1$ , and  $0.45C_1$ . The simulated fractures, which started at a free edge along a perpendicular surface, were driven parallel and close to a free surface. Thus, the effect of the free surface on the dynamic stress field in the vicinity of the fracture tip was determined. The material simulated was assumed to be completely relaxed without any ambient stresses present. Hence, the stresses produced in the model were due to the propagating fracture



tip and the moving pressure source within the fracture surfaces.

As a verification that the code was calculating the effect of the pressure symmetrically on both fracture faces, a calculation was performed with a pressure-driven fracture in the center of the Lagrangian grid. This calculation was terminated before reflections from the grid boundaries parallel to and beyond the fracture tip were reflected back to the fracture. The grid center provided a comparison of the dynamic stresses to show some of the changes due to the rarefaction surface.

Results of the computations are shown in Figures 5a to 15. Three types of data are presented: (1) contour plots of  $|\sigma_1 - \sigma_2|$ , (2) contour plots of dilatation, and (3) plots of the direction of stress tensor. The contour plots of  $|\sigma_1 - \sigma_2|$  and dilatation are heavily shaded around the fracture tip because of the difficulty of describing a surface within the grid with the plotting routines. Interpretation of the contours can be made only outside this heavily shaded area. Plots are presented for two time slices for each of the three fracture velocities. The time slices represent approximately equal times for each fracture velocity, an early time slice with the shorter fracture lengths (Figure 5a through 9a) and a later time slice with the longer fracture lengths (Figure 9b through 13b). Fracture lengths are shown on each plot. The x and y coordinates on the plots have dimensions of centimeters and both the x and y axes shown represent free surfaces for the calculations where the fracture runs parallel to a nearby free surface (x-axis). For the grid center fracture (Figures 14a, 14b, and 15), the y-axis shown represents a free surface and the other surfaces are outside the area of the plot.

Figures 5 through 15 inclusive show the characteristics of the dynamic stress field for the three fracture velocities at the two time slices for each fracture velocity. These plots present the stress field for the fracture near the free surface. Figures 14a, 14b, and 15 show the stress functions for the grid center fracture.

The principal axis of the stress tensor shows the direction of maximum tensile stress. In general, it can be noted from the principal axis plots (Figures 6a, 7b, 9a, 10b, 12a, 13b, and 15) that there is a movement of material from the region in front of the tip toward the tip. The free surfaces, both perpendicular and parallel, allow material between the free surface and the fracture tip to move toward the fracture tip. Except for the fracture velocity of  $0.45C_1$  the orientation of the principal axis indicates that the fracture could travel forward from the tip (Figures 6a, 7b, 10b, and 12a). However, the distortion is much greater at the sides of the fracture adjacent to the pressure source  $|\sigma_1 - \sigma_2|$  than at the tip (Figures 5a, 6b, 9b and 11a). The orientation of the principal axis ahead of the fracture tip for a simulated fracture with a velocity of  $0.45C_1$  is not favorable to forward propagation of the fracture (Figures 9a and 13b). The maximum axis predicts that fractures in front of the tip would be perpendicular to the tip. The time slices for the longer fractures at the lower velocities  $0.25C_1$  and  $0.35C_1$  indicate that the fractures extending forward from the tip would tend to turn toward the free surface (Figures 10b and 12a). For the fracture velocities  $0.25C_1$  and  $0.35C_1$ , the orientation of the principal axes in the material adjacent to the pressure source appears to be controlled by the pressure source. Moreover, examination

of the orientations of the principal axes adjacent to the pressure source shows approximate symmetry about the pressure source, i.e., the free surface has little effect (Figures 6a, 7b, 10b, and 12a).

The contour plots of distortion  $|\sigma_1 - \sigma_2|$  show that the distortion is largely asymmetrical due to the closeness of the free surface on one side of the fracture. In addition, comparison of the distortional contours for the  $0.35C_1$  fracture velocity, between the grid center and nearby free surface fractures (Figures 6b, and 14a), shows that the distortion on the side of the fracture away from the free surface is not greatly affected by the existence of the free surface. The maximum distortion occurs in lobes originating from the fracture faces adjacent to the pressure source (Figures 5a, 6b, 8a, 9b, 11a, and 12b). The maximum magnitude on both sides of the fracture is approximately equal being slightly greater on the side of the fracture adjacent to the free surface.

In general, for all three fracture velocities, the lobe of distortion on the side of the fracture away from the free surface has a larger areal extent than the opposite lobe. Apparently the free surface reduces the size of the distortional lobe but does not effect its magnitude greatly. The distortional contours show a small lobe ahead of the fracture tip, but its magnitude is smaller than that of the side lobes. There is a tendency for the distortional lobe at the tip to be drawn toward the free surface. Behind the crack tip the distortion expands at the dilatational wave speed.

The dilatational contours, in general, show a tendency for the free surface to relax the dilatation. The maximum dilatation occurs just ahead of the fracture tip while two small compressional lobes occur

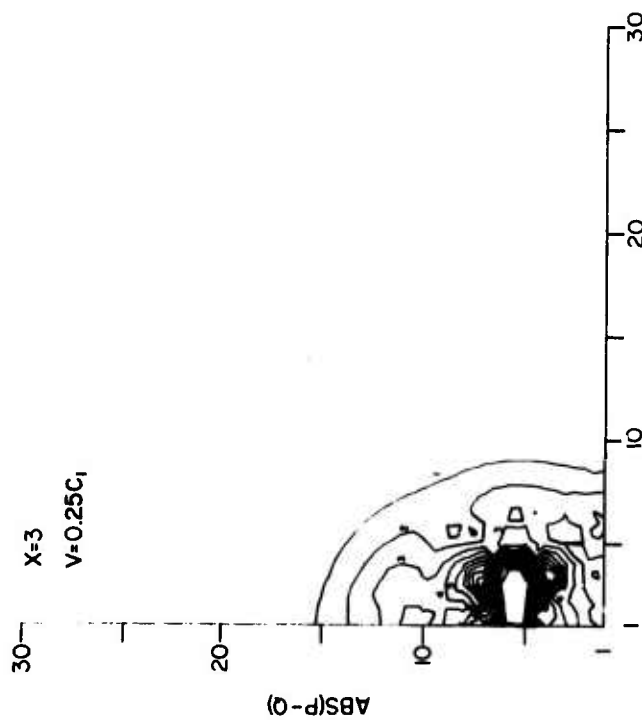


FIGURE 5a The magnitude of the stress difference,  $|\sigma_1 - \sigma_2|$ , for the fracture velocity  $0.25C_1$  and the early time slice. The fracture length is 3 centimeters and the x and y axes on the plot are spatial coordinates in centimeters. The fracture originated at  $x = 1$  and  $y = 5-1/2$  centimeters. The minimum contour (1) is 0.5 and the contour interval is 0.5 kilobar.

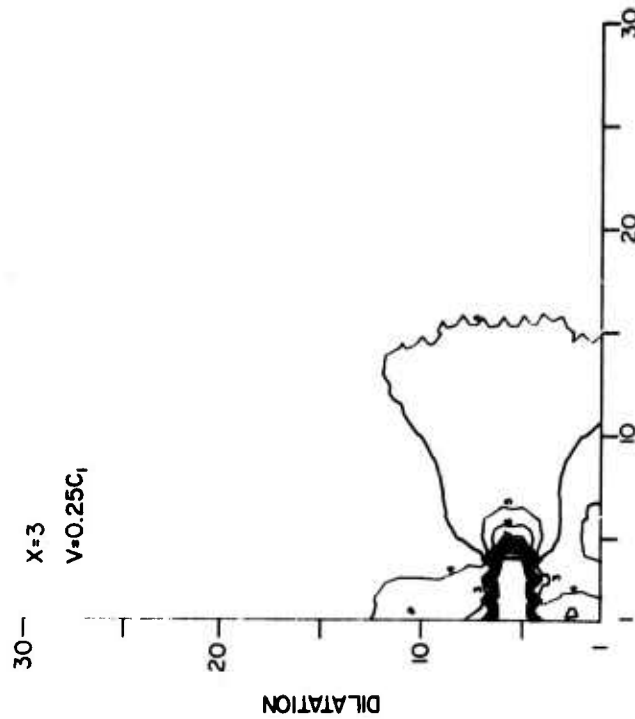


FIGURE 5b The contours of the dilatation for the fracture velocity of  $0.25C_1$  and the early time slice. The fracture length is 3 centimeters and the x and y axes on the plot are spatial coordinates in centimeters. The fracture originated at  $x = 1$  and  $y = 5-1/2$  centimeters. The contour of zero dilatation is 4 with a contour interval of 0.003.

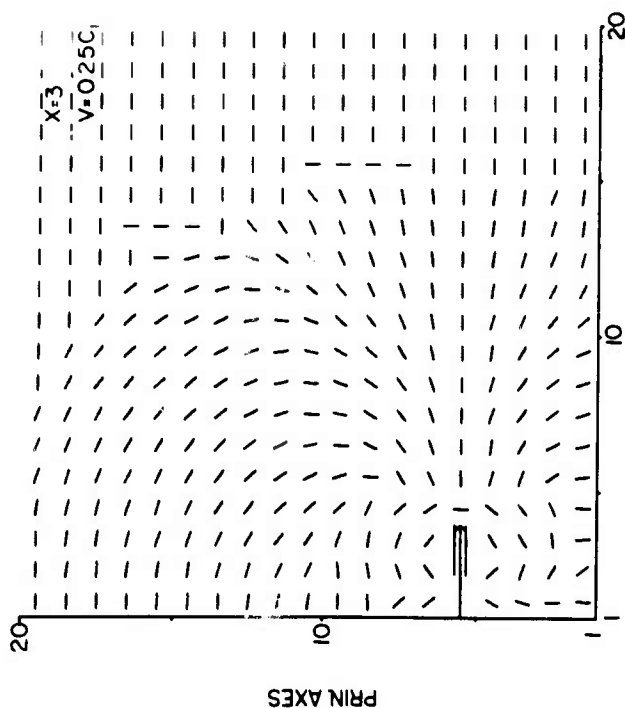


FIGURE 6a

The maximum principal tensor axes for the fracture velocity of 0.25C1 and the early time slice. The fracture length is 3 centimeters and the x and y axes on the plot are spatial coordinates in centimeters. The fracture is shown as the rough line and the position of the pressure source is shown by the double lines, one on each side of the fracture near the tip.

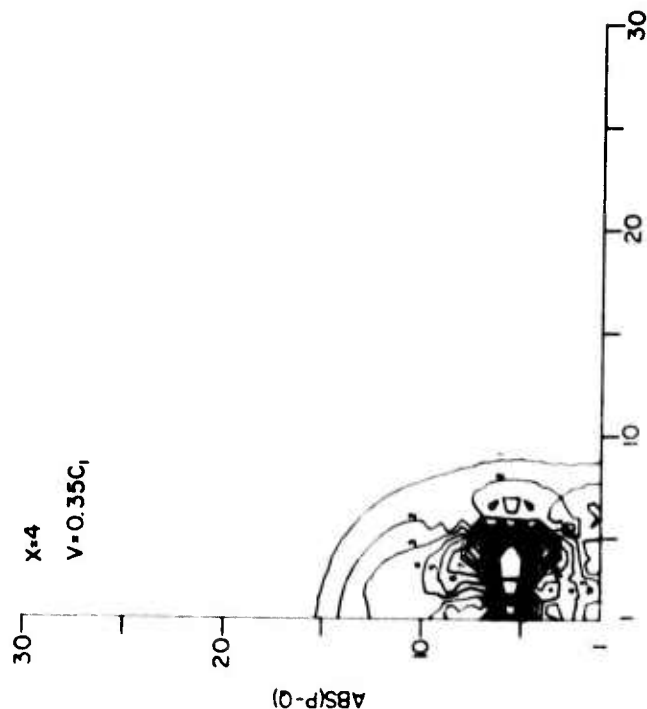


FIGURE 6b

The magnitude of the stress difference,  $|\sigma_1 - \sigma_2|$ , for the fracture velocity 0.35C1 and the early time slice. The fracture length is 4 centimeters and the x and y axes on the plot are spatial coordinates in centimeters. The fracture originated at  $x = 1$  and  $y = 5-1/2$  centimeters. The minimum contour (1) is 0.5 kilobar and the contour interval is 0.5 kilobar.

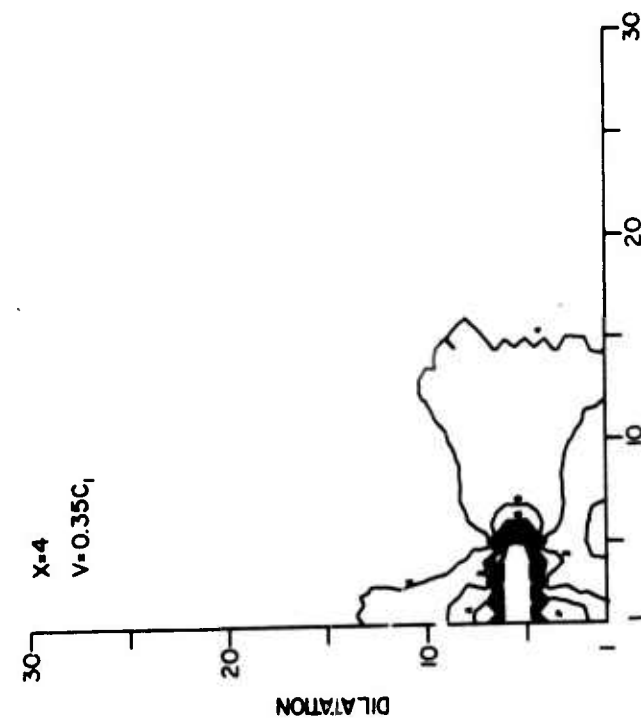


FIGURE 7a

The contours of dilatation for the fracture velocity of  $0.35C_1$  and the early time slice. The fracture length is 4 centimeters and the x and y axes on the plot are spatial coordinates in centimeters. The fracture originated at  $x = 1$  and  $y = 5-1/2$  centimeters. The contour of zero dilatation is 4 with a contour interval of 0.003.

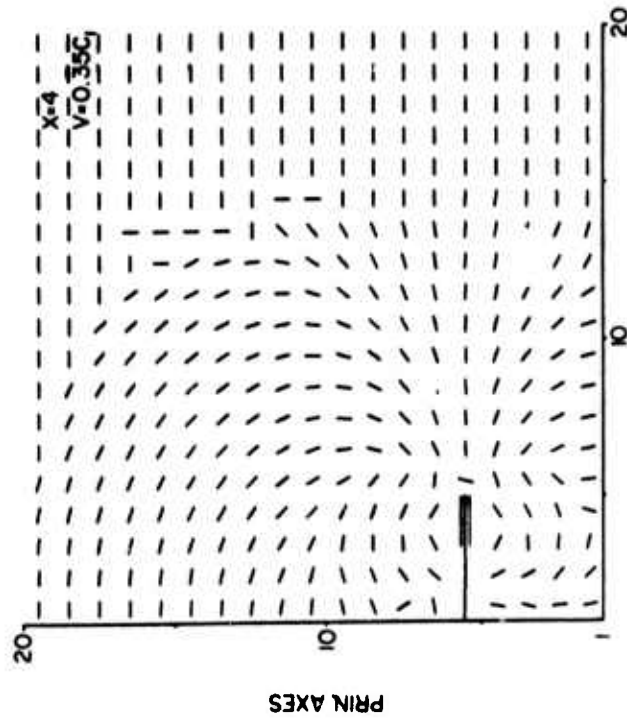


FIGURE 7b

The maximum principal tensor axes for the fracture velocity of  $0.35C_1$  and the early time slice. The fracture length is 4 centimeters and the x and y axes on the plot are the spatial coordinates in centimeters. The fracture is shown as the rough line and the position of the pressure source is shown by the double lines, one on each side of the fracture near the top.

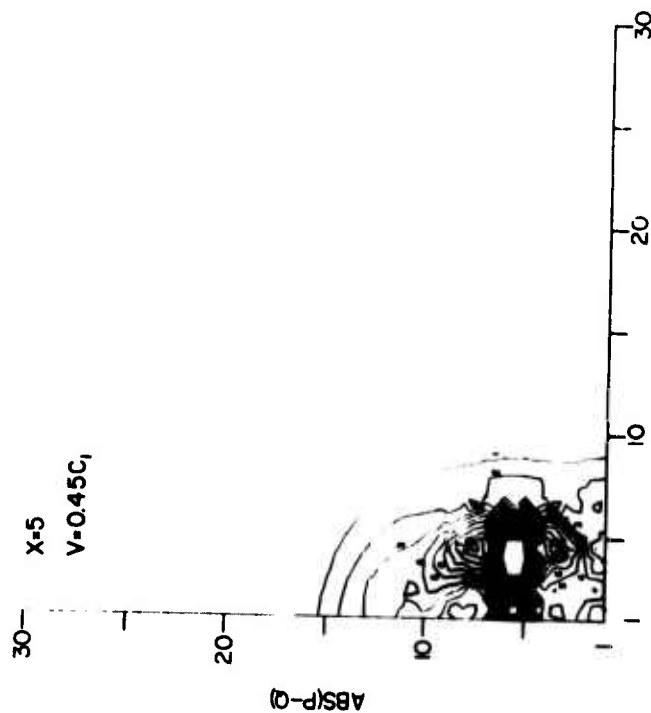


FIGURE 8a

The magnitude of the stress difference  $|\sigma_1 - \sigma_2|$  for the fracture velocity of  $0.45C_1$  and the early time slice. The fracture length is 5 centimeters and the x and y axes on the plots are the spatial coordinates in centimeters. The fracture originated at  $x = 1$  and  $y = 5-1/2$  centimeters. The minimum contour (1) is 0.5 kilobar and the contour interval is 0.5 kilobar.

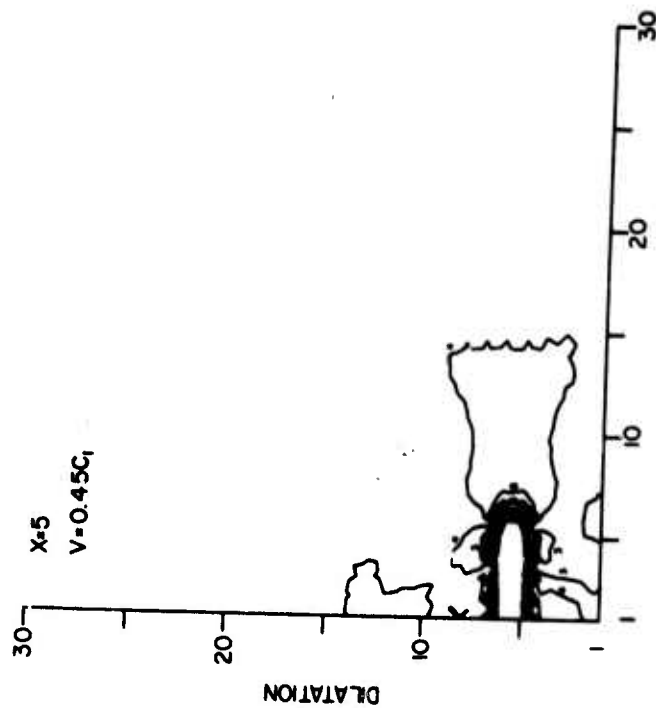


FIGURE 8b

The contours of dilatation for the fracture velocity of  $0.45C_1$  and the early time slice. The fracture length is 5 centimeters and the x and y axes on the plot are spatial coordinates in centimeters. The fracture originated at  $x = 1$  and  $y = 5-1/2$  centimeters. The contour of zero dilatation is 4 and the contour interval is 0.003.

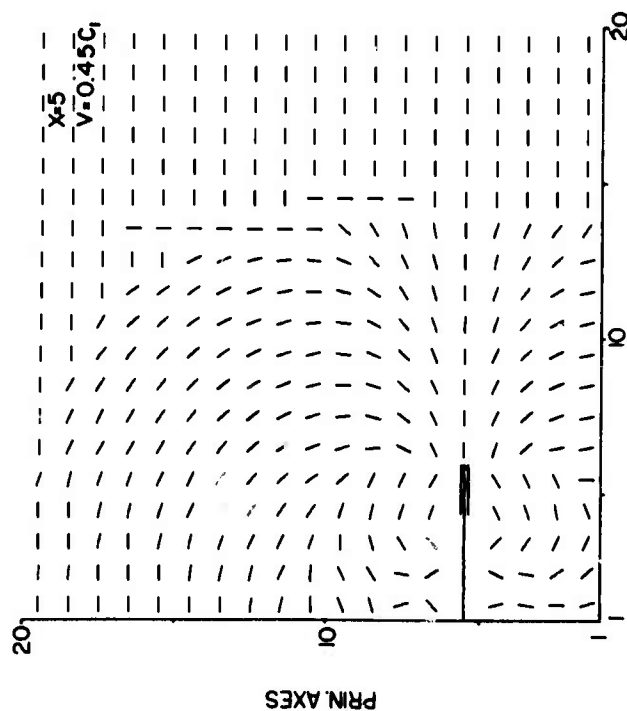


FIGURE 9a

The maximum principal tensor axes for the fracture velocity of  $0.45C_1$  and the early time slice. The fracture length is 5 centimeters and the x and y axes on the plot are the spatial coordinates in centimeters. The fracture is shown as the rough line and the position of the pressure source is shown by the double lines, one on each side of the fracture near the tip.

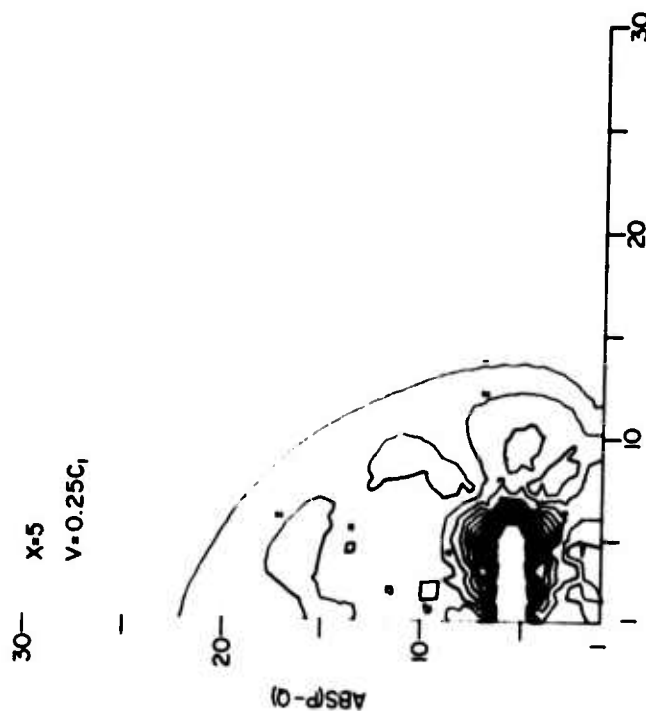


FIGURE 9b

The magnitude of the stress difference,  $|\sigma_1 - \sigma_2|$ , for the fracture velocity of  $0.25C_1$  and the later time slice. The fracture length is 5 centimeters and the x and y axes on the plot are the spatial coordinates in centimeters. The fracture originated at  $x = 1$  and  $y = 5-1/2$  centimeters. The minimum contour (1) is 0.5 kilobar and the contour interval is 0.5 kilobar.



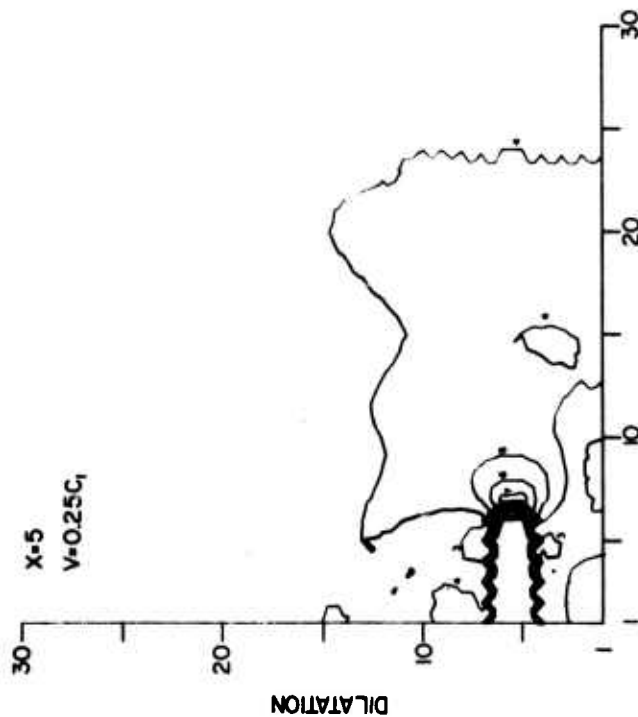


FIGURE 10a  
The contours of dilatation for the fracture velocity of  $0.25C_1$  and the later time slice. The fracture length is 5 centimeters and the  $x$  and  $y$  axes on the plot are the spatial coordinates in centimeters. The fracture originated at  $x = 1$  and  $y = 5-1/2$  centimeters. The contour of zero dilatation is 4 and the contour interval is 0.003.

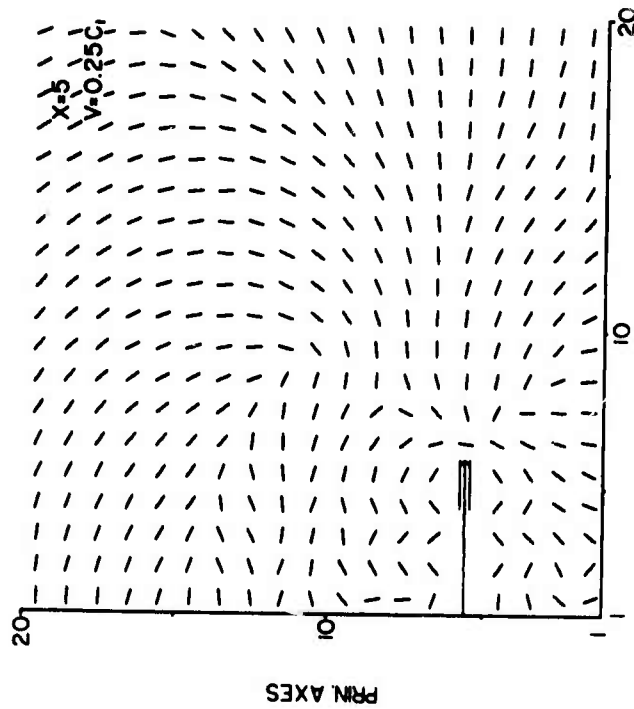


FIGURE 10b  
The maximum principal tensor axes for the fracture velocity of  $0.25C_1$  and the later time slice. The fracture length is 5 centimeters and the  $x$  and  $y$  axes on the plot are the spatial coordinates in centimeters. The fracture is shown as the rough line and the position of the pressure source is shown by the double lines, one on each side of the fracture near the tip.

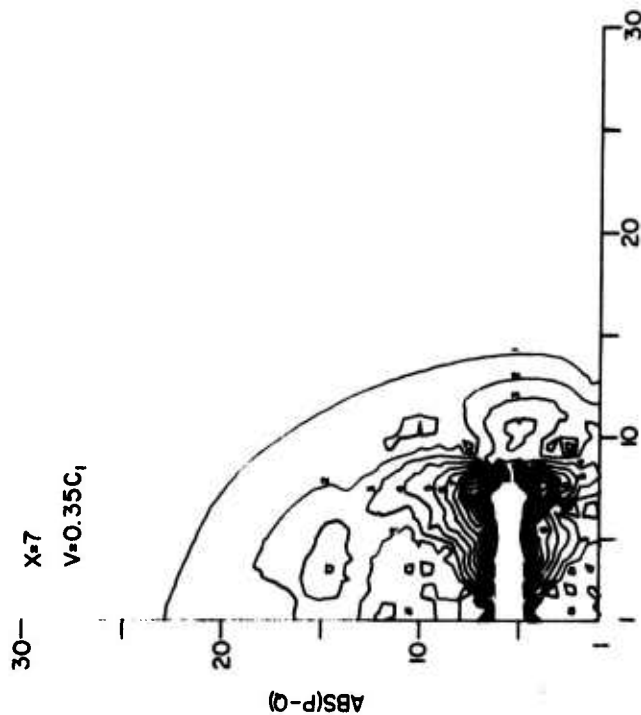


FIGURE 11a  
The magnitude of the stress difference  $|\sigma_1 - \sigma_2|$  for the fracture velocity of  $0.35C_1$  and the later time slice. The fracture length is 7 centimeters and the x and y axes on the plot are the spatial coordinates in centimeters. The fracture originated at  $x = 1$  and  $y = 5-1/2$  centimeters. The minimum contour (1) is 0.5 kilobar and the contour interval is 0.5 kilobar.

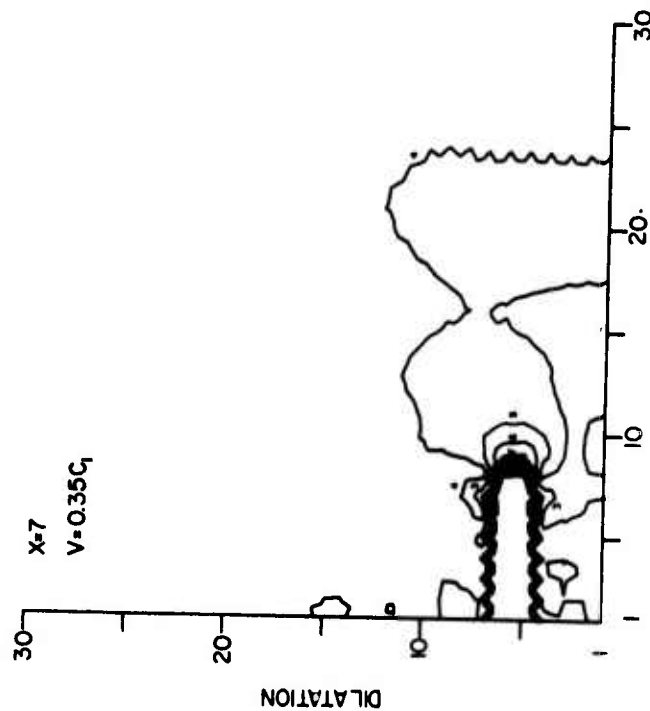


FIGURE 11b  
The contours of dilatation for the fracture velocity of  $0.35C_1$  and the later time slice. The fracture length is 7 centimeters and the x and y axes on the plot are the spatial coordinates in centimeters. The fracture originated at  $x = 1$  and  $y = 5-1/2$  centimeters. The contour of zero dilatation is 4 and the contour interval is 0.003.

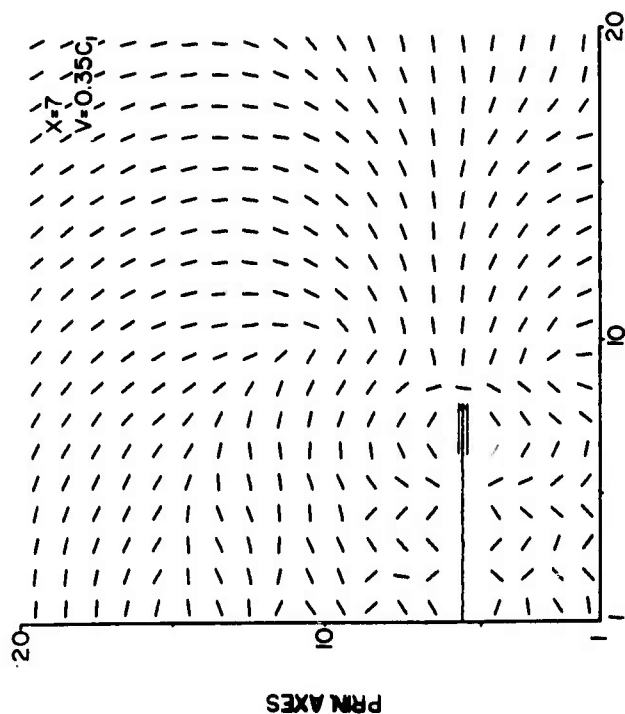


FIGURE 12a

The maximum principal tensor axes for the fracture velocity of  $0.35C_1$  and the later time slice. The fracture length is 7 centimeters and the x and y axes on the plot are the spatial coordinates in centimeters. The fracture is shown as the rough line and the position of the pressure source is shown by the double lines, one on each side of the fracture near the tip.

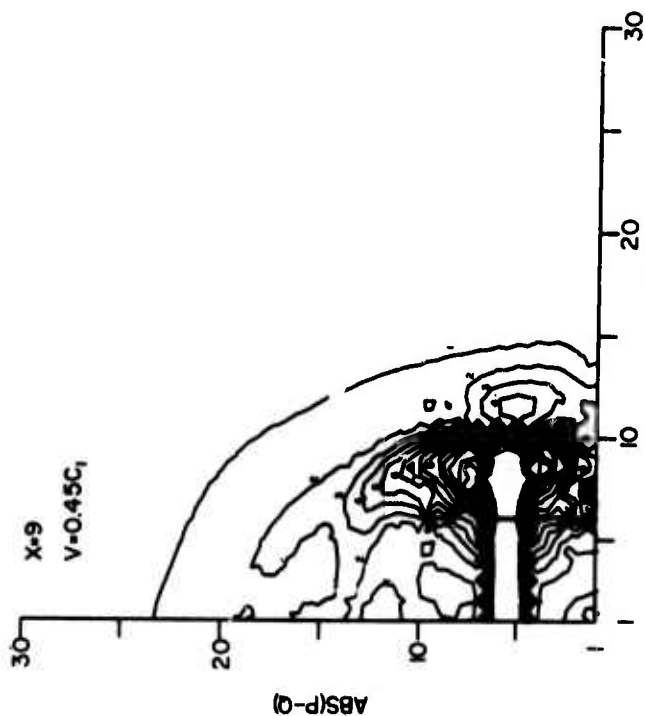


FIGURE 12b

The magnitude of the stress difference,  $|\sigma_1 - \sigma_2|$ , for the fracture velocity of  $0.45C_1$  and the later time slice. The fracture length is 9 centimeters and the x and y axes on the plot are the spatial coordinates in centimeters. The minimum contour (l) is 0.5 kilobar and the contour interval is 0.5 kilobar.

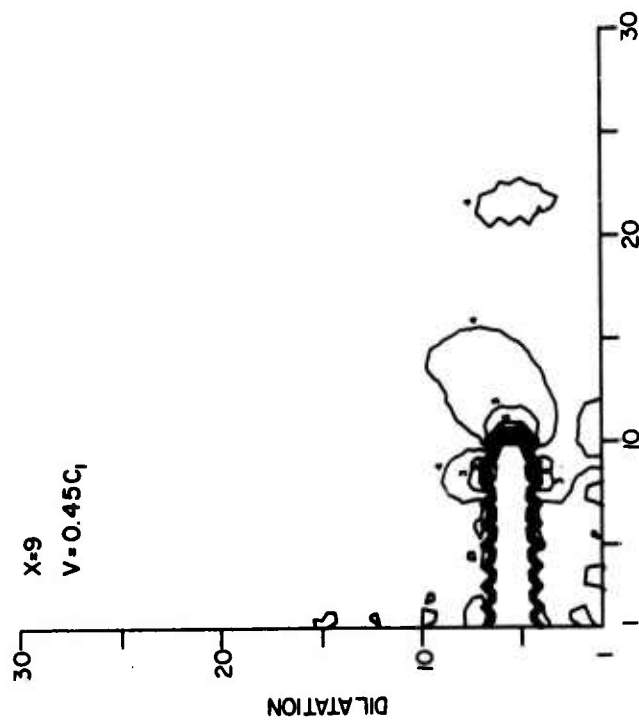


FIGURE 13a  
The contours of dilatation for the fracture velocity of  $0.45C_1$  and the later time slice. The fracture length is 9 centimeters and the x and y axes on the plot are the spatial coordinates in centimeters. The fracture originated at  $x = 1$  and  $y = 5-1/2$  centimeters. The contour of zero dilatation is 4 and the contour interval is 0.003.

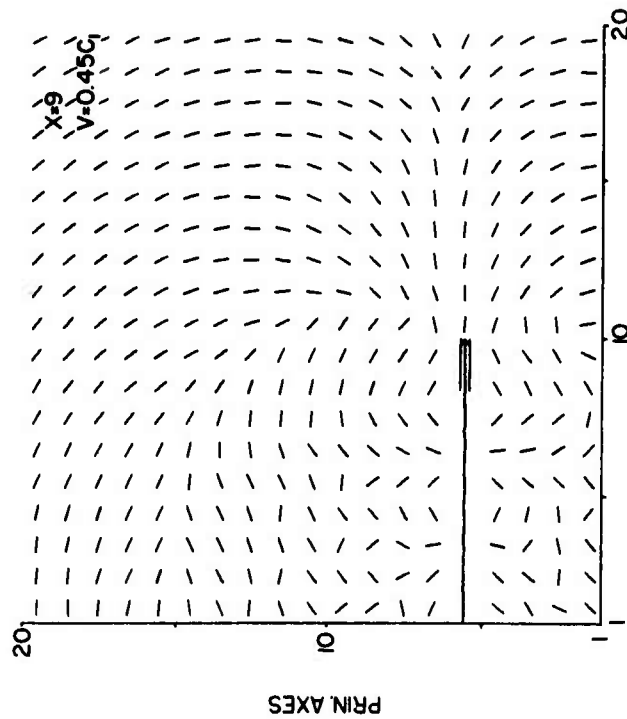


FIGURE 13b  
The maximum principal tensor axes for the fracture velocity of  $0.45C_1$  and the later time slice. The fracture length is 9 centimeters and the x and y axes on the plot are the spatial coordinates in centimeters. The fracture is shown as the rough line and the position of the pressure source is shown by the double lines, one on each side of the fracture near the tip.

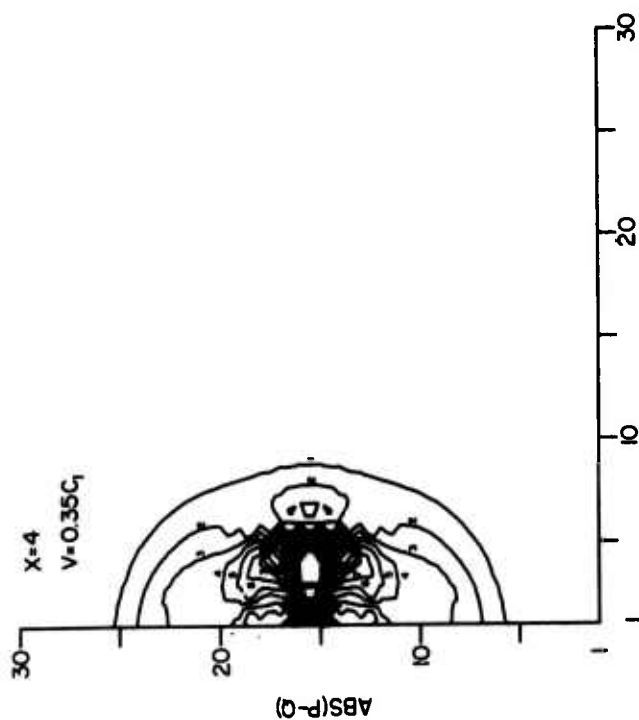


FIGURE 14a  
The magnitude of the stress difference,  $|\sigma_1 - \sigma_2|$ , for the grid center fracture at the early time slice and a fracture velocity of  $0.35C_1$ . The fracture length is 4 centimeters and the x and y axes on the plot are the spatial coordinates in centimeters. The fracture originated at  $x = 1$  and  $y = 15-1/2$  centimeters. The minimum contour (1) is 0.5 kilobar and the contour interval is 0.5 kilobar.

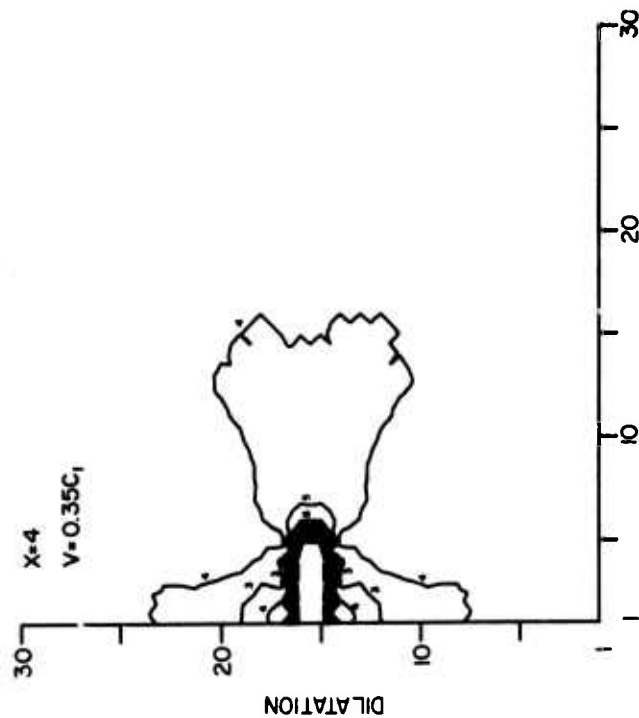


FIGURE 14b  
The contours of dilatation for the grid center fracture at the early time slice and a fracture velocity of  $0.35C_1$ . The fracture length is 4 centimeters and the x and y axes on the plot are the spatial coordinates in centimeters. The fracture originated at  $x = 1$  and  $y = 15-1/2$  centimeters. The contour of zero dilatation is 4 and the contour interval is 0.003.

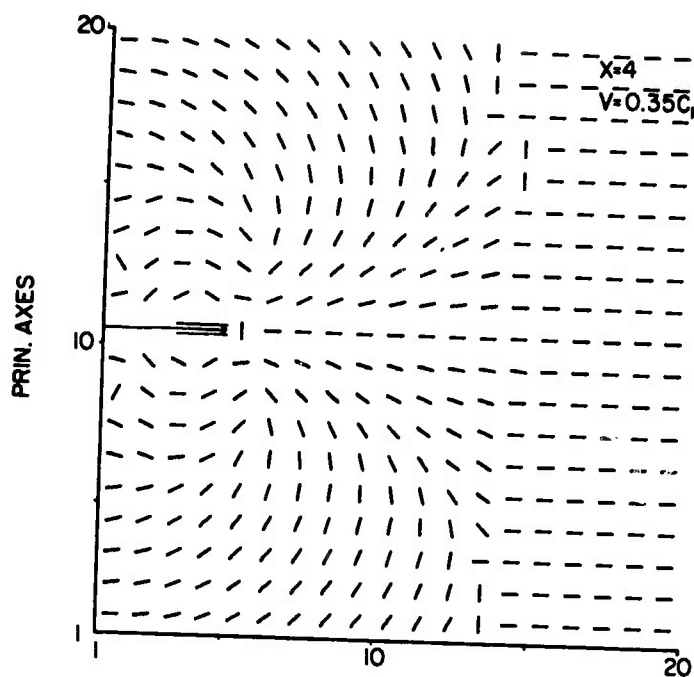


FIGURE 15

The maximum principal tensor axes for the grid center fracture at the early time slice and a fracture velocity of  $0.35C_1$ . The fracture length is 4 centimeters and the x and y axes on the plot are the spatial coordinates in centimeters. The fracture is shown as the rough line and the position of the pressure source is shown by the double lines, one on each side of the fracture near the tip.

behind the tip adjacent to the pressure source (Figures 5b, 7a, 8b, 10a, 11b, and 13a). The compressional lobe away from the free surface has a larger areal extent than the one toward the free surface. The two slower velocities result in the dilatational lobe ahead of the fracture having a larger areal extent than does the fracture of velocity  $0.45C_1$ . All the later time slice contour plots of dilatation (Figures 10a, 11b, and 13a) show a dilatation (at about  $y = 15$ ) from a Rayleigh wave travelling along the free surface.

### C. SUMMARY AND CONCLUSIONS

The results indicate that a pressure-driven fracture in an ideal, homogeneous, isotropic material at velocities of  $0.45C_1$  is not physically possible. At this velocity, the orientation of the maximum tensile stress ahead of the fracture tip indicates that new fractures in this region would occur perpendicular to the existing fracture. This agrees with the results of the research shown in Reference 1. It is possible but not probable that this result could be changed by the inclusion of branch fractures.

It is not physically realistic to define fracturing to occur in a straight line at a constant velocity. To do so implies that the stresses in the region of the fracture tip are ignored. However, the analysis had to be applied in this manner in the absence of more sophisticated fracture formulations. The analysis was performed to show the character of the elastic field in the vicinity of the fracture and the moving pressure source. The effect of the nearby free surface on the dynamic elastic field was also obtained in the results.

The free surface parallel to the fracture tends to relax the dilatation resulting from the moving fracture and pressure. This can be noted by the fact that the dilatational lobes are skewed away from the free surface and the compression lobe is drawn toward the surface. Since the maximum magnitude of the distortion on both sides of the moving fracture behind the tip are approximately equal, apparently the distortion is created and held by the pressure source and the moving fracture tip.

The plots of the orientation of the principal axes indicate that if maximum tensile stress controls the direction of fracture ahead of the moving fracture tip, the fractures would turn toward the nearby free surface. In addition, the plots indicate that the orientation of the principal axes on each side of the fracture is controlled by the pressure source. Since the distortion is also maximum in these regions, fractures created near the pressure source would initially be symmetric and away from the original fracture. The free surface would not affect the initial orientation of the branch fractures. Since an electron beam has a finite diameter on the surface, any branch fracture originating in the beam areas would also be pressurized. The pressurization of these branch fractures would remove the parallel tensile field in the vicinity of the forward tip. If the orientation of the branch fractures is sufficiently symmetric, then it may be possible to drive a fracture tip parallel to a free surface. Hence, with sufficient beam power, a mining application can be envisioned.

It should be restated that these tentative conclusions are drawn from a two-dimensional analysis.



## SECTION IV

### EXPERIMENTAL RESULTS

#### A. DESCRIPTION OF EXPERIMENTS

More than 50 individual experiments were performed previous to those performed on the three large sawed granite blocks. These experiments were used to establish the amount of explosive necessary to initiate a fracture and to establish the best method to slow the linear velocity of detonation of the explosive cord. All experiments performed were passive in that no dynamic instrumentation was used on the test specimen. Interpretations of the test were made through observation of fractures after the test. Within the observational capability of the experimental method used, it was determined that the amount of explosive per unit length on the test specimen necessary to initiate a fracture was about the same as that required to propagate the fracture.

A major factor in causing fracture to occur in a specimen is the ability to transfer the available energy of the detonation and the explosive gases to the specimen in an orientation which will result in the desired fracture. The cord had to be taped to the surface of the test specimen to hold it in its snaked configuration and some open space existed between the cord and buffers and the stemming material. Obtaining the same amount of energy coupling to the specimen for different experiments was difficult because of the texture of the stemming material used and the relative amount of water contained in the mud. The method of snaking the cord was found to be the most feasible way of slowing the linear velocity of propagation of detonation to simulate a high-power electron beam moving along a hard rock surface at fracture velocity.

The experiments using a slower linear velocity were limited to certain velocities due to the size of cord available. First, to allow legitimate comparisons, the cord was snaked at a ratio of three (four or five) units of cord per linear unit. Then three (four or five) cords were placed straight beside each other to supply the same energy-density per unit length so a comparison could be made between experiments having the two velocities. An alternate method for obtaining the higher velocity at the same energy-density per unit length was achieved by allowing the detonation wave to bridge in the snaked cord. The latter method produced about the same damage as when the cords were placed straight beside each other.

Figures 16a through 23b show the results of detonating PETN Primacord over a length of 0.6 meters. Figures 16a, 17a, and 18a show the damage produced by about 2000 grains per meter (600 grains per foot) of explosive, placed along a 0.61-meter length, with the velocity of fracture propagation (V) about 2100 meters per second. The cord was snaked in a width less than .05 meter and centered 4 inches (0.10 meter) from the edge. The pieces broken from the specimens, or those indicated by visible cracks resemble each other and appear triangular in cross section and about as long as the length of the snaked cord (0.6 meter).

Figure 16b, 17b, and 18b show the damage produced by the same explosive density as for the previous figures but the velocity of propagation here is that of the explosive cord (about 6,400 meters per second). The propagation velocity is supersonic in the test specimen. Figure 16b shows the characteristic width of the spallation slabs which

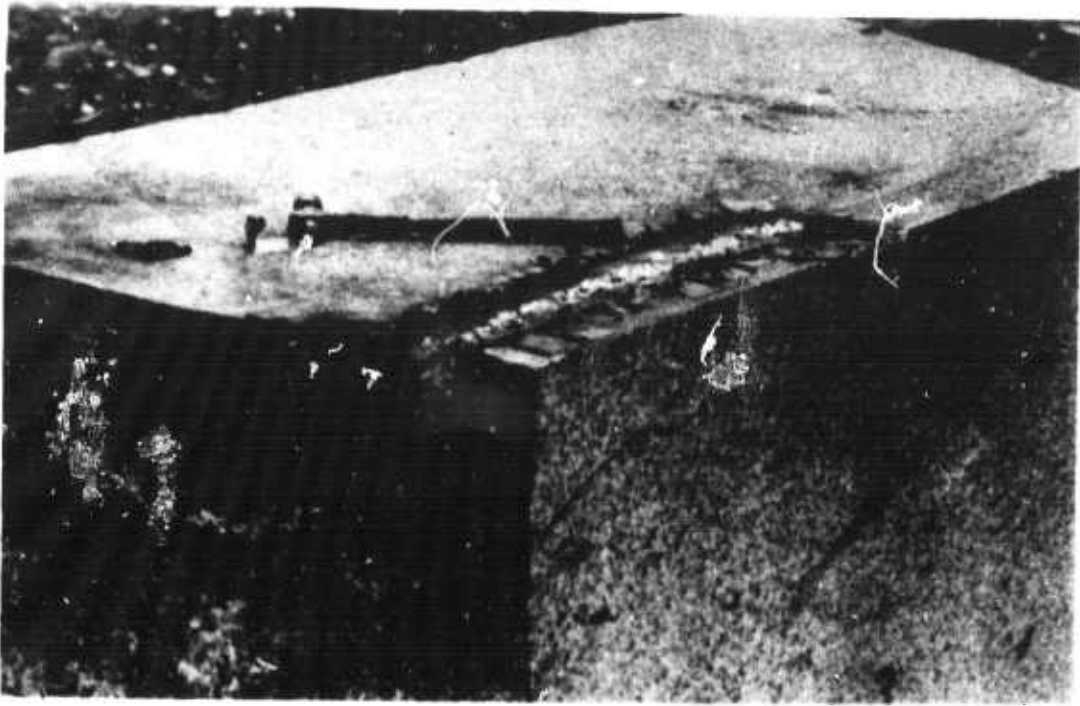


FIGURE 16a. Explosive density was 2000 grains/meter with V equal to 2100 meters/second.

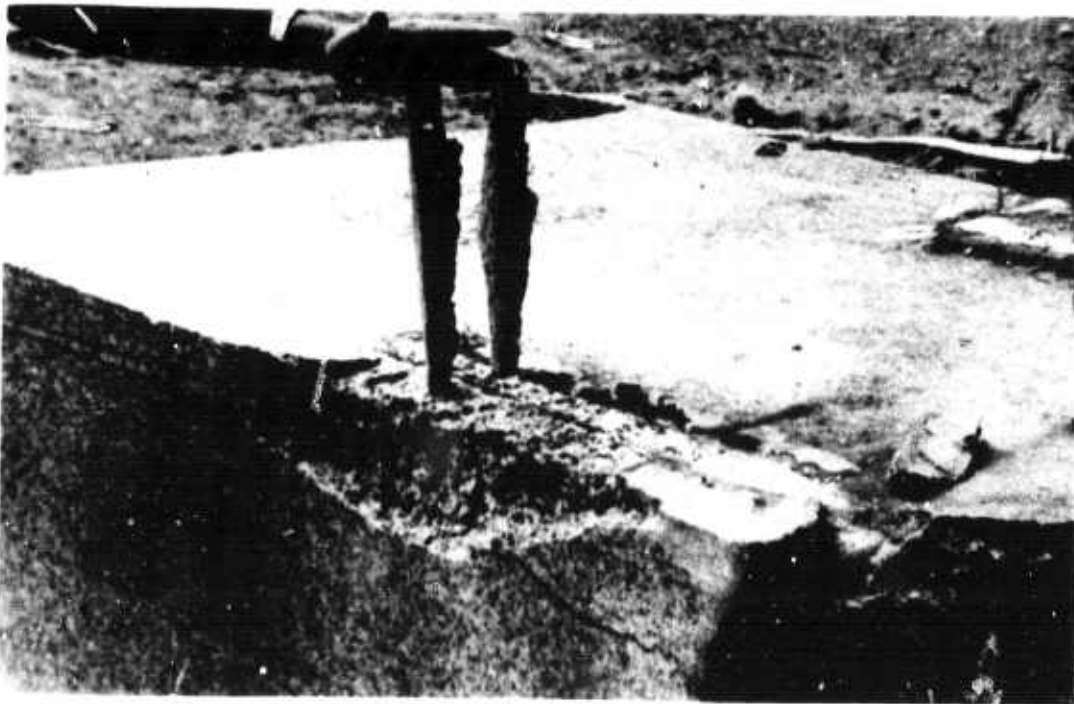


FIGURE 16b. Explosive density was 2000 grains/meter with V equal to 6400 meters/second.



FIGURE 17a. Explosive density was 2000 grains/meter with V equal to 2100 meters/second.

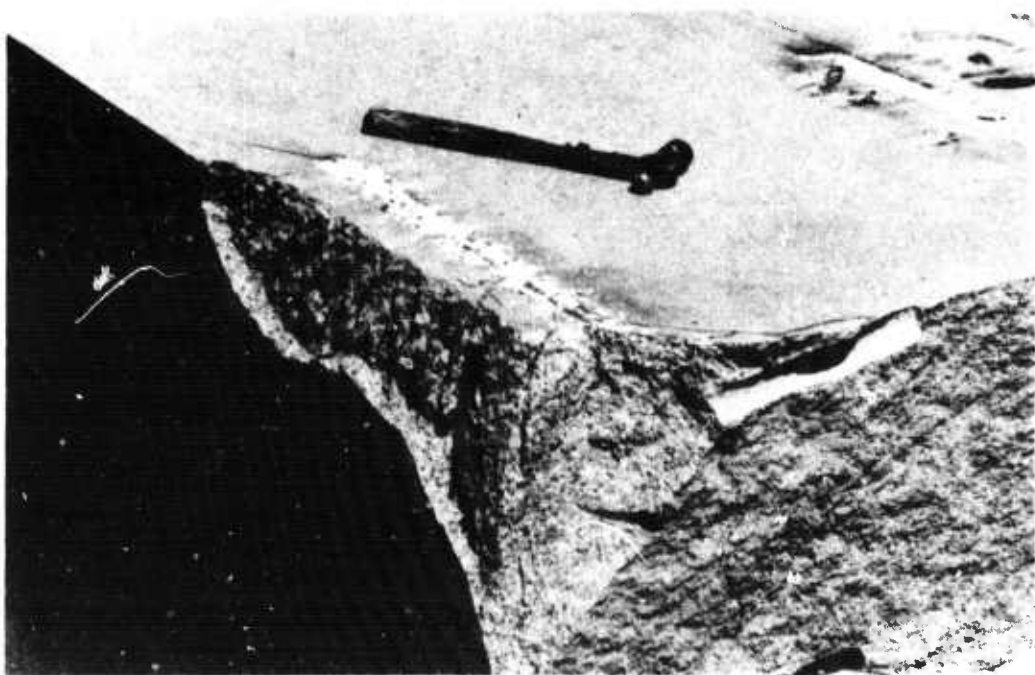


FIGURE 17b. Explosive density was 2000 grains/meter with V equal to 6400 meters/second.

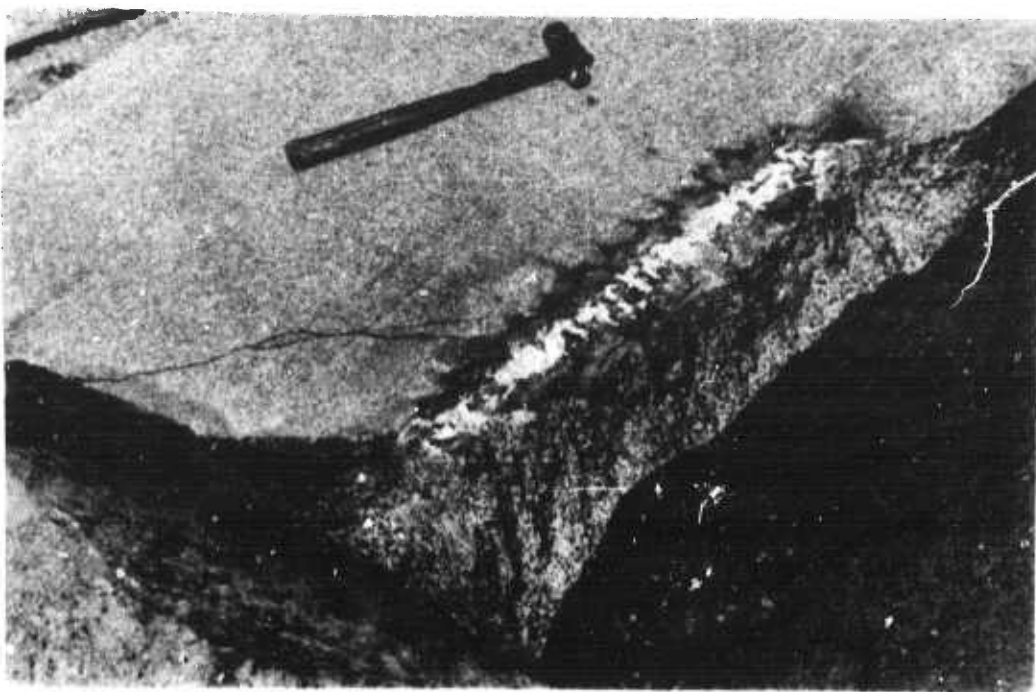


FIGURE 18a. Explosive density was 2000 grains/meter with V equal to 2100 meters/second.

Reproduced from  
best available copy.

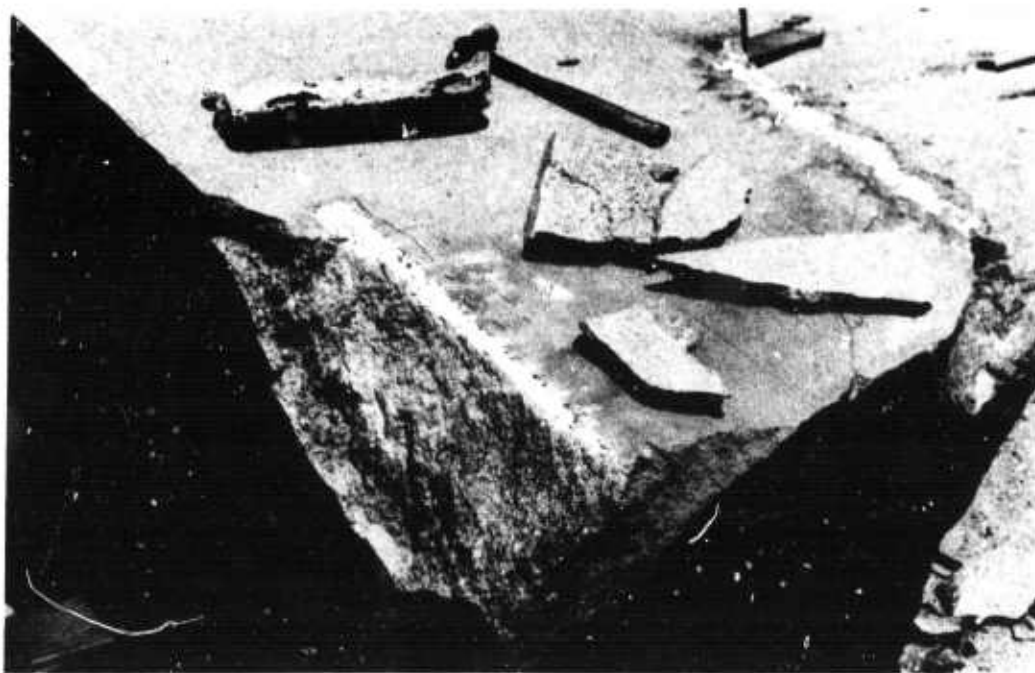


FIGURE 18b. Explosive density was 2000 grains/meter with V equal to 6400 meters/second.

is about the same width as the explosive used. Figures 17b and 18b show spallation damage caused by supersonic detonation velocities. Figure 18b shows a lot of separation, but much of it was due to imperfections in the specimen which were visible (as discolorations along the fracture surfaces) after breaking.

Figures 19a, 20a, and 21a show the damage produced by a propagation velocity of 1600 meters per second and an explosive density of 2600 grains per meter. Comparison of these three figures with Figures 16a, 17a, and 18a suggests that a higher explosive density and a slower propagation velocity does not increase the damage to the specimens. Figure 20a shows hardly any damage.

The damage shown in Figures 19b and 20b was caused by an explosive density of 2600 grains per meter and a propagation velocity of 6400 meters/second. The experiment shown in Figure 19b can be compared with the one Figure 16b (same velocity but explosive density of 2000 grains per meter). There is little difference in the damage produced by these two shots. Figure 20b indicates the supersonic detonation can do more damage than the subsonic detonation on the same block (Figure 20a).

Figure 21b shows four independent detonations at 6400 meters/second with explosive density of 2600 grains per meter. The side shown in Figure 20b is opposite the side of the block used in the experiments shown on Figures 16a, 16b, 19a, and 19b. Notice the large chunks broken out of the near corners. We suspect the fractures that created these large pieces of granite were partially formed during the previous shots. Also some evidence of pre-existing fractures was found. The four shots shown all exhibit a deep spallation.

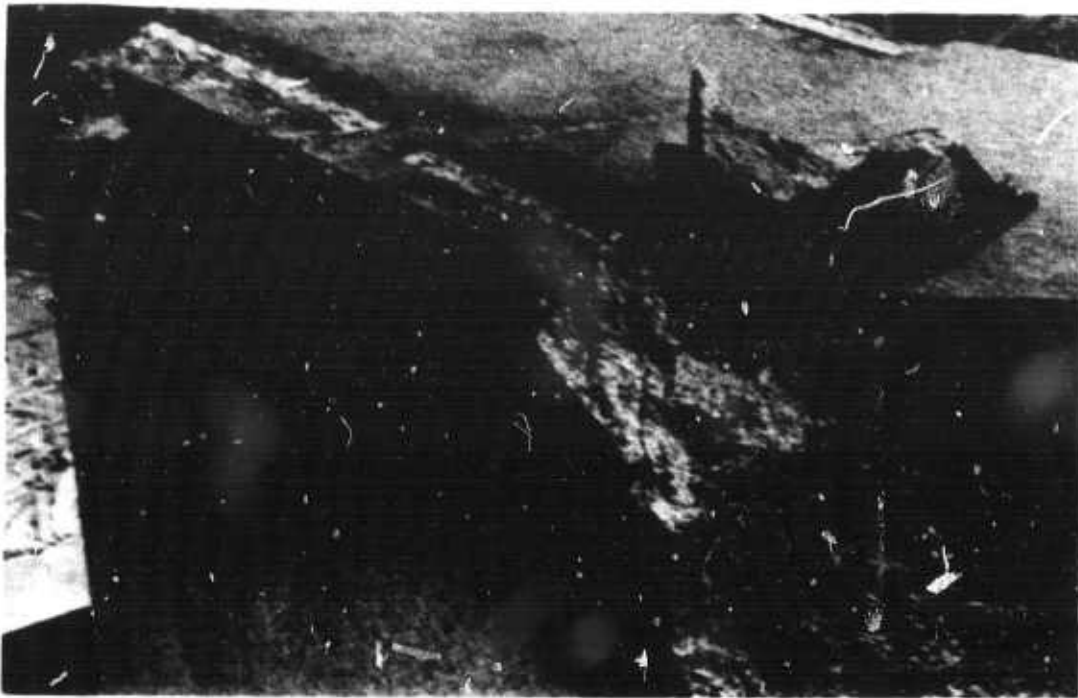


FIGURE 19a. Explosive density was 2600 grains/meter with V equal to 1600 meters/second.

Reproduced from  
best available copy.

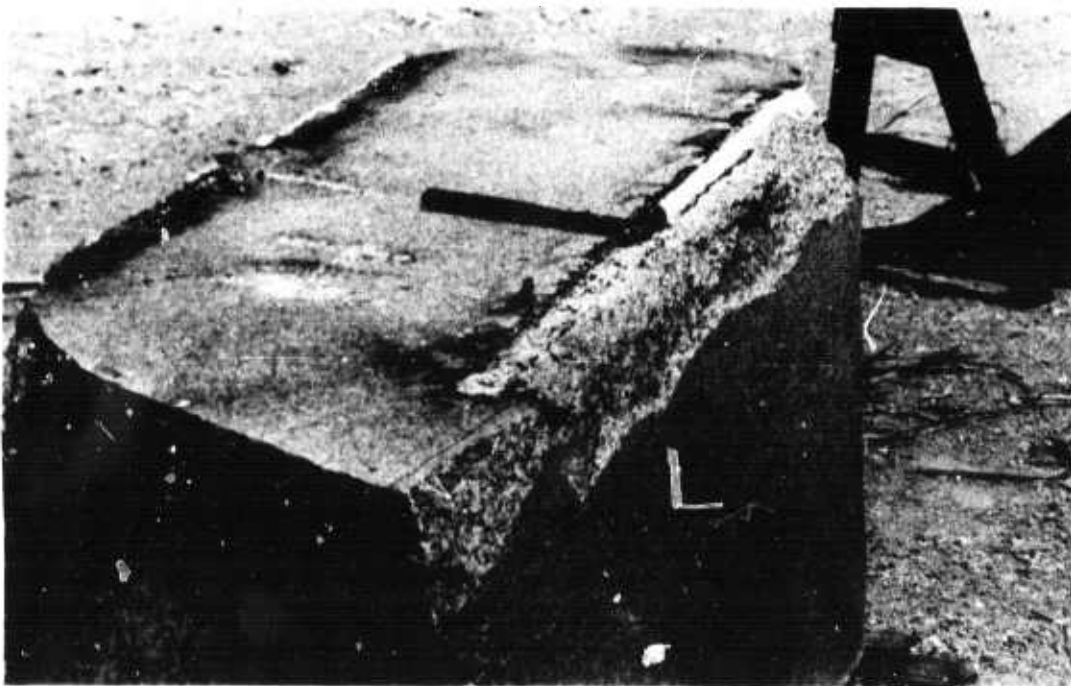


FIGURE 19b. Explosive density was 2600 grains/meter with V equal to 6400 meters/second.



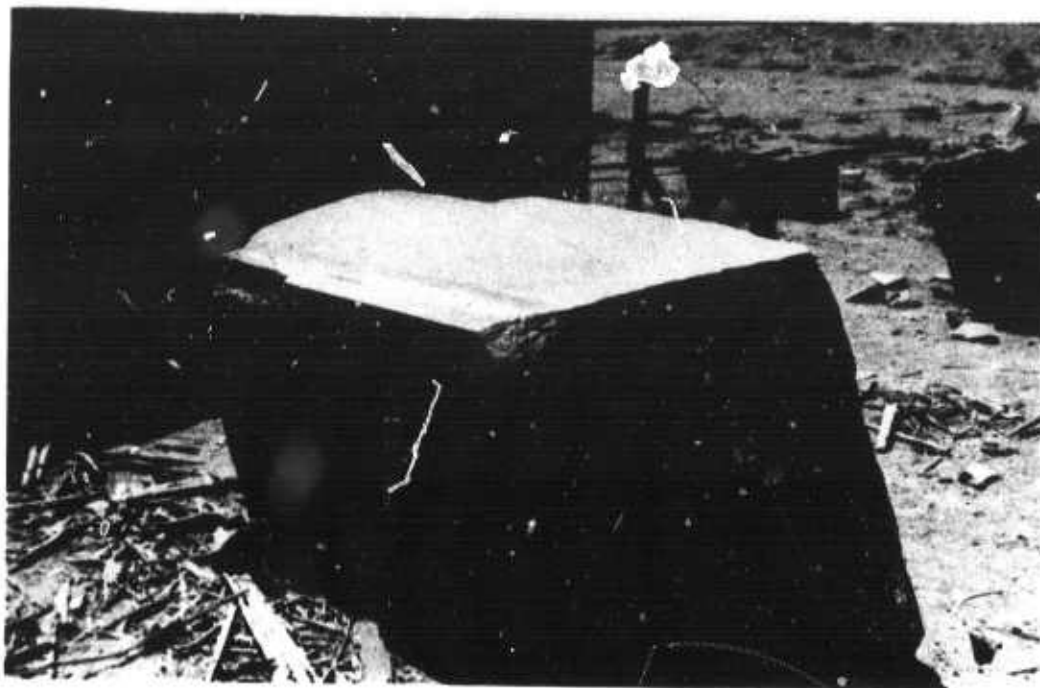


FIGURE 20a. Explosive density was 2600 grains/meter with V equal to 1600 meters/second.

Reproduced from  
best available copy.



FIGURE 20b. Explosive density was 2600 grains/meter with V equal to 6400 meters/second.



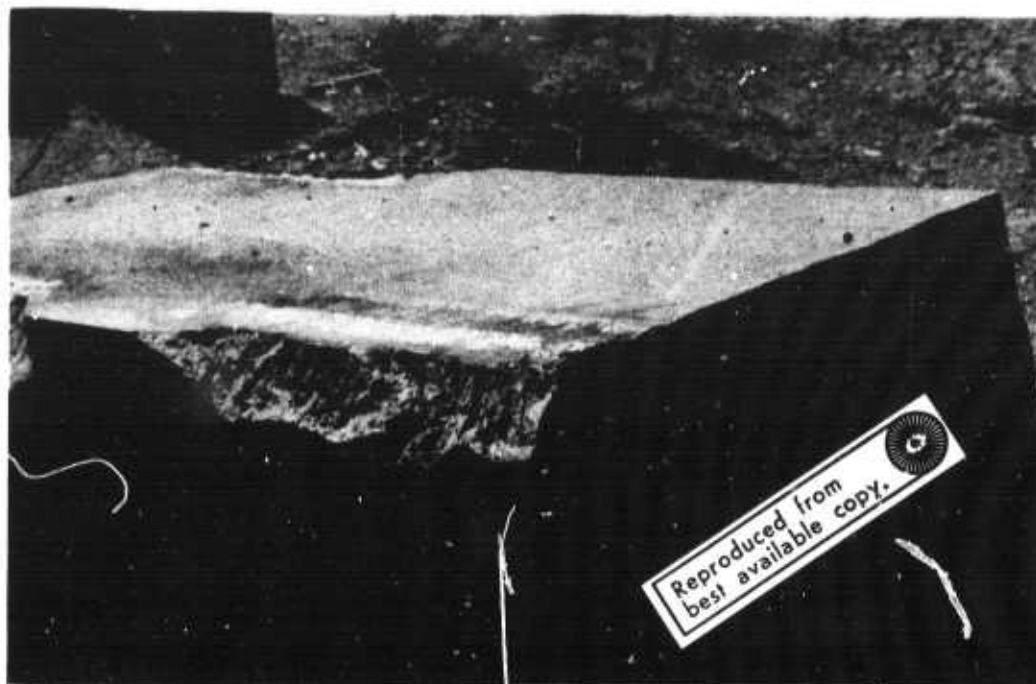


FIGURE 21a. Explosive density was 2600 grains/meter with V equal to 1600 meters/second.

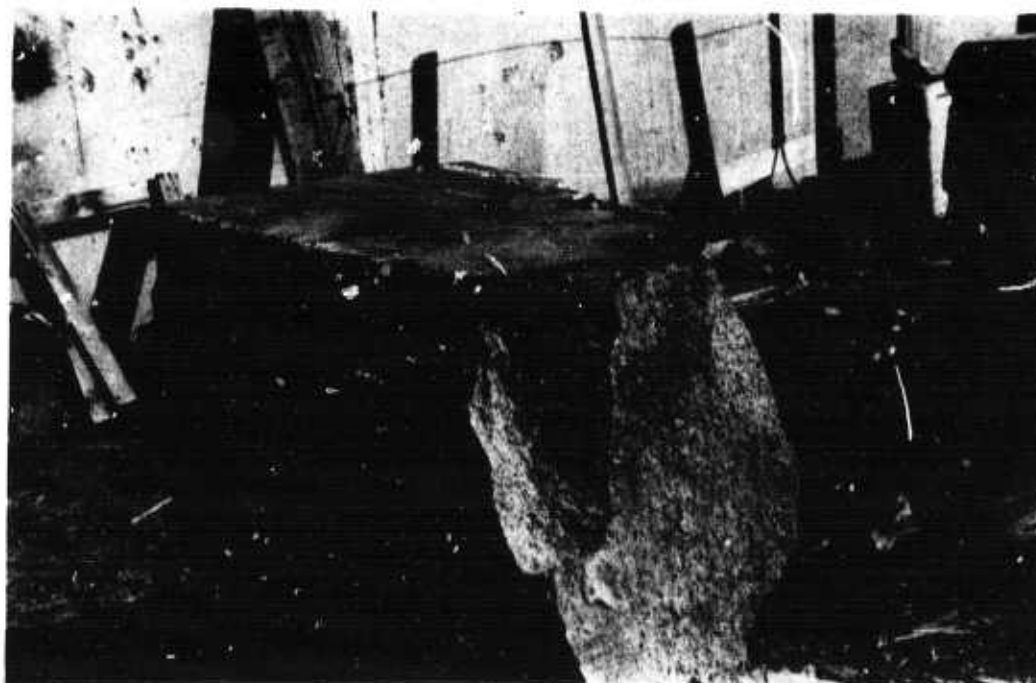


FIGURE 21b. Explosive density was 2600 grains/meter with V equal to 6400 meters/second.

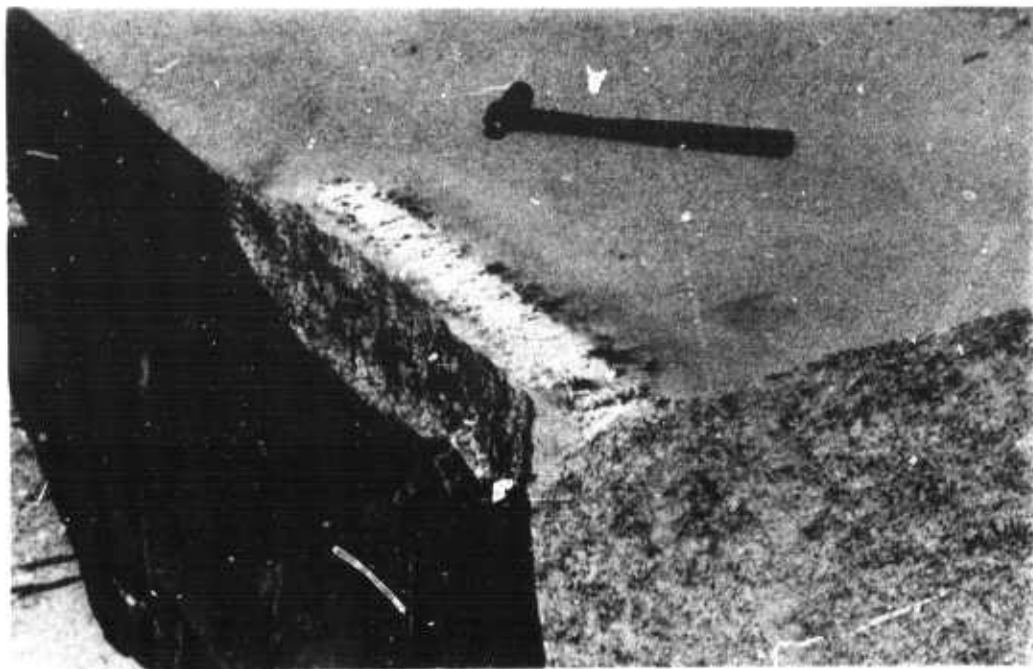


FIGURE 22a. Explosive density was 1600 grains/meter with V equal to 5000 meters/second.

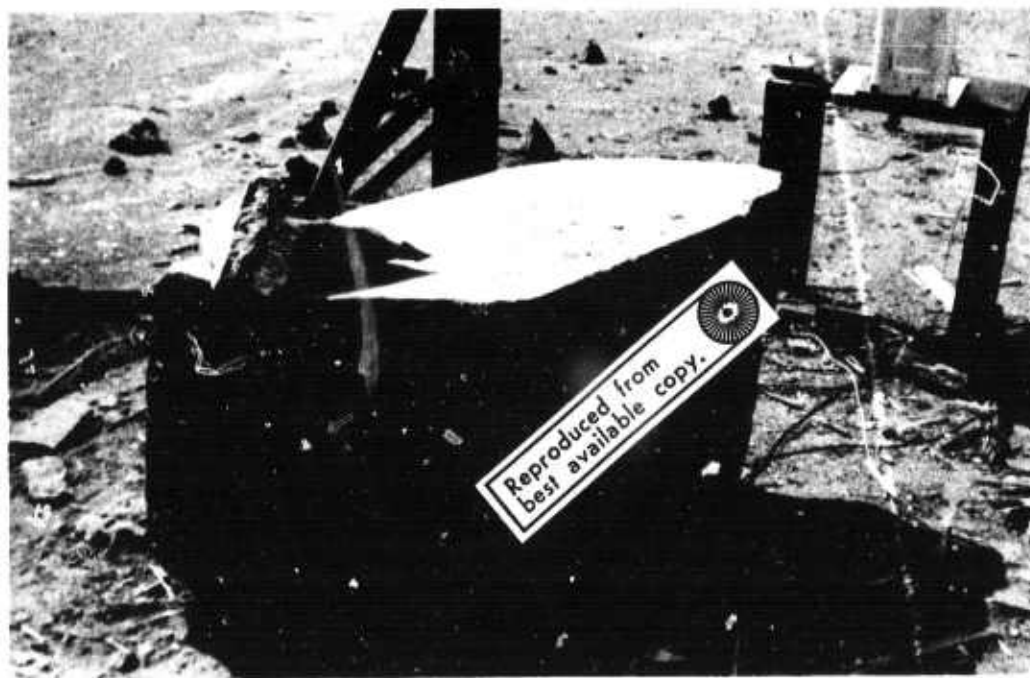


FIGURE 22b. Explosive density was 1600 grains/meter with V equal to 1300 meters/second.

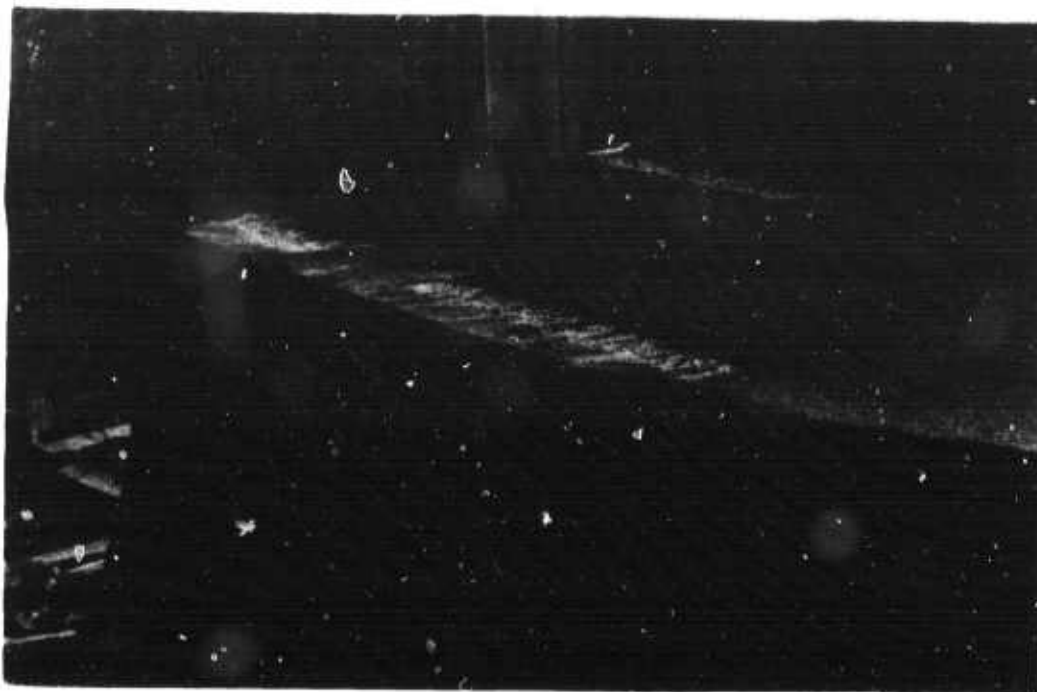


FIGURE 23a. Explosive density was 1600 grains/meter with V equal to 1300 meters/second.

Reproduced from  
best available copy.

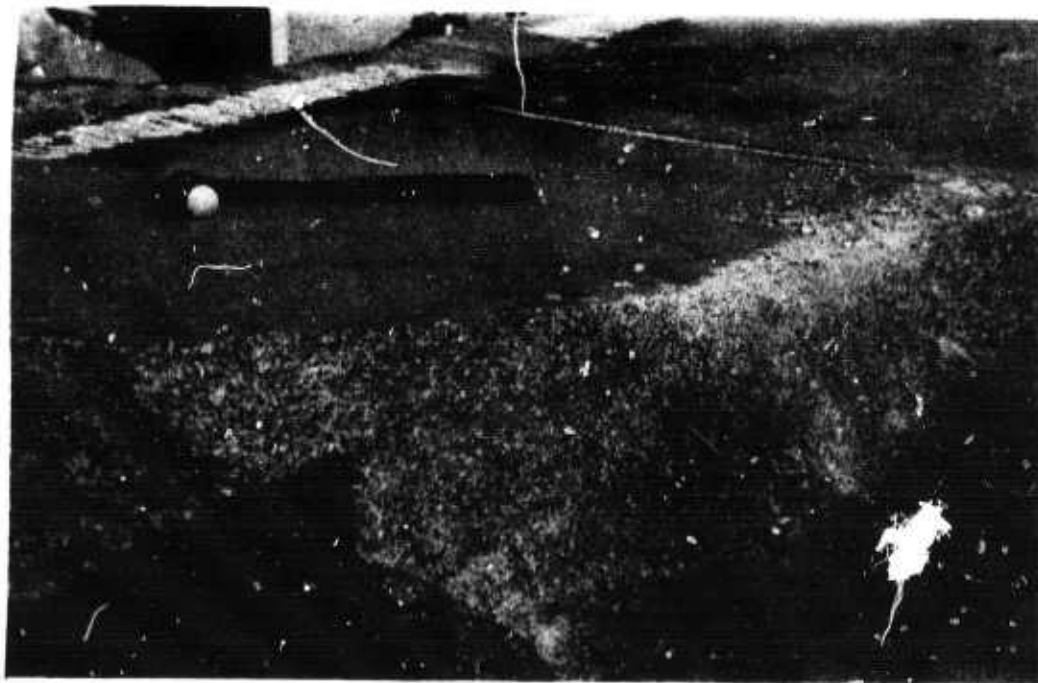


FIGURE 23b. Explosive density was 1600 grains/meter with V equal to 1300 meters/second.

Figure 22a illustrates the results of a shot made with an energy-density of 1600 grains per meter. The cord was snaked but enough bridging did occur to cause the average detonation velocity to become greater than the velocity of P-waves in the specimen, hence the spallation.

Figures 22b, 23a, and 23b show results of experiments using a detonation velocity of 1300 meters per second at an energy-density of 1600 grains per meter. Figure 23a shows no visible damage while Figures 22b and 23b show a large piece of the specimen broken from the corners at which the detonations were initiated. Again we caution that some of this fracturing may have occurred from experiments performed on the other side of the block where higher explosive densities were used. Note the pieces that were broken off at supersonic detonation velocities (Figure 21b) were not of the tetrahedral shape of those shown in Figures 22b and 23b. Also no discolorations indicating pre-existing fractures were evident in these two experiments. The broken piece of granite shown in Figure 22b and the block shown in Figure 23b both exhibit fractures which could be the branch fractures described in the theoretical part of this study.

#### B. DISCUSSION AND CONCLUSIONS OF EXPERIMENTS

Very little research has been conducted on the creation of fractures by placing explosive cord on a hard rock surface. Some published literature does contain analytical and experimental results for explosive geometries quite different than those used in this study. Previous investigators (References 9, 10) have experimentally studied

the effects of different types of explosives placed internally in granite. Some of the earliest analytical work was by Sharpe (Reference 11) who studied the elastic waves produced from an internal pressure source on a spherical cavity. This is the simplest geometry available (one-dimensional) for analysis if the mechanisms of explosive loading on the internal surface are neglected. Subsequent experimentalists (Reference 12) found that shock loading phenomena must be taken into account on the explosive-rock interface. In addition, elastic wave observations (Reference 13) indicated the ratio of the rock impedance to the explosive impedance (product of the density and detonation velocity) was a governing parameter in rock breakage applications. Although these studies involved internally placed explosives, some of the results could be applicable to the methods used in our analysis.

Duvall and Atchison (Reference 14) describe the explosive breaking of rock as two mechanisms. In the first mechanism, the rock near the detonation point is crushed by the high pressure of the explosive gases. Their analysis was for explosive contained in a borehole and crushing would be expected to occur. Detonation of explosive on a free surface exhibits only a small amount of crushing. In the second mechanism, the compressional wave is reflected at a free boundary as a tension wave and rock breakage occurs as tensile failure. The conclusions of their study indicate that the position and orientation of a dynamic fracture would depend entirely upon the free boundaries of the specimen. Some results of this research do not appear to agree with their conclusions.

Many of the experiments performed for this research resulted in breaking directly under the line where the cord was detonated. This result indicates that the free surfaces do not geometrically define fracture in all cases. We interpreted our results as an indication that the ambient stress field in the specimen may have some effect on the geometry of the fracture, and that the fracture was driven directly from the explosive source rather than from secondary effects.

In nearly all cases, fracture occurred directly below the explosive. However, the extent of the fracturing was difficult to observe. In many experiments explosive cord was detonated near an edge and fractures were not observed below the detonation line. However, additional detonations at a similar distance from the previous shots caused observable fractures to appear where the previous shots were made.

## SECTION V

### SUMMARY

Difficulties in evaluating the results of this research arise because of the differences between the analyses and experiments performed. The analyses were for a two-dimensional block with the moving source placed within the fracture surfaces. The experiments had a three-dimensional geometry with the source placed on a free surface near an edge. The fact that the explosive cord used in the experiments was placed on a free surface makes a direct quantitative comparison between the theory and experiment difficult. Also in the experiments, the explosive energy coupled to the specimen was unknown and is of major importance in breaking rock.

There can be serious questions raised as to whether an electron beam can be simulated by using an explosive detonating cord because of the detonation shock from the explosive. Further, the energy from an electron beam is deposited a few crystal depths into the surface of a specimen in comparison with the energy from an explosive which is coupled into the surface through the detonation shock and the residual gas pressure after the shock. The impedance characteristics of the detonation products and the test material have to be considered to understand the coupling of the explosive energy to the test specimen. On the other hand, the thermodynamic properties of the test material should be considered to understand the effect of the electron beam. The deposition of the beam energy, if large enough, will result in an ablation of the test material with the resultant ablation pressure being the working mechanism to drive the fracture.

The characteristic pressure width resulting from the detonation of the explosive cord was 5 cm; whereas, the width of the electron beam applied within the fracture surfaces in the analyses was less than 1 cm. Also the pressure wave in the experiments was mainly coupled downward into the face, while the pressure in the analyses was applied outward against the fracture faces.

Despite these difficulties, some similarities between the experiments and the analyses appear to exist. There is evidence from some of the experiments that branch-type fractures have occurred. The relaxation to the free surface from which the fracture was started (seen in the tensor axis plots, Figures 6a, 7b, (9a), 10b, 12a, and 13b) shows up as severe damage on the same face in the experiments. The cumulative damage below the line where the explosive was detonated on the surface of the test specimen is an indication that a pressure can result in some fracturing near the pressure source.

The analyses indicated that the pressure source, if applied within the fracture surfaces, can "hold" the stress orientation such that the orientation of branch fractures would be symmetrical. Since the distortion is large in the region of the pressure source, branch fractures will occur and pressurization of the branch fractures could reduce the effects of the free surface so that a fracture may be driven parallel to the free surface.



## REFERENCES

1. Hanson, M. E.; A. R. Sanford, "Some Characteristics of a Propagating Brittle Tensile Crack," Geophys. J., 23, 1971.
2. Dulaney, E. N.; W. F. Brace, "Velocity Behaviour of a Growing Crack," J. Appl. Phys., 31, 1960.
3. Wells, A. A.; D. Post, "The Dynamic Stress Distribution Surrounding a Running Crack--a Photoelastic Analysis", Spring Meeting of the Society for Experimental Stress Analysis, Boston, Mass., 1957.
4. Bieniawsky, Z. T., "The Phenomenon of Terminal Fracture Velocity in Rock", Rock Mech. and Engr. Geol., 6, 1968.
5. Bieniawsky, Z. T., "Fracture Dynamics of Rock", Intern. Jour. of Fracture Mech., 4, 1968.
6. Petschek, A. L.; M. E. Hanson, "Difference Equations for Two-Dimensional Elastic Flow", J. Comp. Phys., 3, 1968.
7. Hanson, M. E.; A. R. Sanford, "A Two-Dimensional Source Function for a Dynamic Brittle Bilateral Tensile Crack", Bull. Seis. Soc. of Amer., 60, 1970.
8. Hanson, M. E.; A. R. Sanford; A. J. Shaffer, "A Source Function for a Dynamic Bilateral Brittle Shear Fracture", J. Geophys. Res. 76, 1971.
9. Atchison, T. C.; W. E. Tournay, "Comparative Studies of Explosives in Granite", Bureau of Mines Report of Investigations 5509, 1959.
10. Atchison, T. C.; J. M. Pugliese, "Comparative Studies of Explosives in Granite-Second Series of Tests", Bureau of Mines Report of Investigations 6434, 1964.
11. Sharpe, J. A. "The Production of Elastic Waves by Explosion Pressure--I, Theory and Empirical Field Observations", Geophysics, 7, No. 2, 1942.
12. Sadwin, L. D.; S. Okubo; J. E. Kennedy, "Explosive Performance as Related to Blasting", Fifth Symposium on Rock Mechanics, University of Minnesota, Pergamon Press, New York, 1963.
13. Nichols, H. R.; W. I. Duvall, "Effect of Characteristic Impedance on Explosion-Generated Strain Pulses on Rock", Fifth Symposium on Rock Mechanics, University of Minnesota, Pergamon Press, New York, 1963.
14. Duvall, W. I.; T. C. Atchison, "Rock Breakage by Explosives", Bureau of Mines Report of Investigations 5356, 1957.

UNCLASSIFIED

Security Classification

## DOCUMENT CONTROL DATA - R &amp; D

(Security classification of title, body of abstract and indexing annotation must be entered when the overall report is classified)

1. ORIGINATING ACTIVITY (Corporate author) New Mexico Institute of Mining and Technology Socorro, New Mexico 87801		2a. REPORT SECURITY CLASSIFICATION Unclassified	
		2b. GROUP	
3. REPORT TITLE ELECTRON BEAM FRACTURING OF HARD ROCK			
4. DESCRIPTIVE NOTES (Type of report and inclusive dates) 13 October 1970 through 13 December 1971			
5. AUTHOR(S) (First name, middle initial, last name) Merle E. Hanson, Ronald J. Shaffer, and Allan R. Sanford			
6. REPORT DATE February 1972	7a. TOTAL NO. OF PAGES 54	7b. NO. OF REFS 14	
8a. CONTRACT OR GRANT NO. F29601-71-C-0017	8b. ORIGINATOR'S REPORT NUMBER(S) AFWL-TR-71-143		
b. PROJECT NO.			
c. ARPA Order Number 1690	9b. OTHER REPORT NO(S) (Any other numbers that may be assigned this report)		
d.			
10. DISTRIBUTION STATEMENT Distribution limited to US Government agencies only because of test and evaluation (February 1972). Other requests for this document must be referred to AFWL (SYS), Kirtland AFB, NM 87117.			
11. SUPPLEMENTARY NOTES		12. SPONSORING MILITARY ACTIVITY AFWL (SYS) Kirtland AFB, NM 87117	
13. ABSTRACT (Distribution Limitation Statement B) An experimental and analytical investigation has been conducted to determine if a moving pressure source can drive a fracture parallel to a free surface. The research was conducted to determine the technical feasibility of a hard-rock mining technique using a high-energy electron beam to create the moving pressure source. By controlling the electron beam sweep orientation and sweep velocity across a rock face, a minimum-energy rock-breaking procedure can be envisioned. The two-dimensional analytical technique used could not simulate fracture branching phenomena. However, the analysis of the dynamic stress field produced by a programmed straight fracture did indicate that branch fractures would occur in the region of the pressure source. If these branch fractures were subsequently pressurized, it might be possible to propagate the fracture parallel to the free surface. The experimental investigations showed 1) that slowing the detonation velocity does cause different fracture characteristics but does not necessarily increase the amount of damage; 2) that fracture always occurred to some extent directly below the line of detonation (perpendicular to the free surface) where pressure was applied; 3) that explosive detonating cord probably cannot be used to simulate a high energy electron beam; and 4) that a ripple type detonation will not produce sufficient energy on the surface of the test specimen. The detonating cord had to be applied in a snaked geometry on the surface to provide the slow phase velocities and the high energy densities. Some correlation between experiment and analysis can be made in the branch fracture pattern and the damage on the fracture initiation surface.			

UNCLASSIFIED

Security Classification

14	KEY WORDS	LINK A		LINK B		LINK C	
		ROLE	WT	ROLE	WT	ROLE	WT
	Dynamic fracture mechanics Simulation of earthquakes Electron beam cutting of hard rock						

UNCLASSIFIED

Security Classification

**THIS REPORT HAS BEEN DELIMITED  
AND CLEARED FOR PUBLIC RELEASE  
UNDER DOD DIRECTIVE 5200.20 AND  
NO RESTRICTIONS ARE IMPOSED UPON  
ITS USE AND DISCLOSURE.**

**DISTRIBUTION STATEMENT A**

**APPROVED FOR PUBLIC RELEASE,  
DISTRIBUTION UNLIMITED.**